Chapter 2
Morphology of Different Electrodeposited Pure Metal Powders

V.D. Jović, N.D. Nikolić, U.Č. Lačnjevac, B.M. Jović, and K.I. Popov

2.1 Introduction

As mentioned in other chapters, metal powders obtained by electrolytic processes are mainly dendrites which can spontaneously fall off or can be removed from the electrode by tapping or other similar techniques [1]. Also, powder particles can have other morphological forms, such as flakes or needles, fibrous or spongy, and needle or

V.D. Jović (✉) • U.Č. Lačnjevac • B.M. Jović
Department of Materials Science, Institute for Multidisciplinary Research,
University of Belgrade, Kneza Višeslava 1, 11030 Belgrade,
P.O. Box 33, Serbia
e-mail: vladajovic@imsi.rs; uros.lacnjevac@imsi.rs; bjovic@imsi.rs

N.D. Nikolić
ICTM-Institute of Electrochemistry, University of Belgrade,
Njegoseva 12, P.O.B. 473, 11001 Belgrade, Serbia
e-mail: nnikolic@tmf.bg.ac.rs

K.I. Popov
ICTM-Institute of Electrochemistry, University of Belgrade,
Njegoseva 12, P.O.B. 473, 11001 Belgrade, Serbia

Faculty of Technology and Metallurgy, University of Belgrade,
Karnegijeva 4, P.O.B. 3503, 11001 Belgrade, Serbia
e-mail: kosta@tmf.bg.ac.rs

cauliflower-like ones, and the shape of powder particles depends on the electrodeposition conditions and the nature of the metal.

Some technologically and academically important metal powders, such as copper, silver, nickel, cobalt, lead, and cadmium, are obtained by electrolysis of aqueous solutions.

According to Winand [2], metals can be classified into three groups:

(a) Normal metals (Cd, Zn, Sn, Ag (silver nitrate solutions), Pb) which have low melting points, T_m, and high exchange current densities, j_0
(b) Intermediate metals [Au, Cu, Ag (silver ammonia complex)], which have moderate T_m and medium j_0
(c) Inert metals (Fe, Ni, Co, Pt, Cr, Mn), which have high T_m and low j_0

The aim of this chapter is morphological analysis of some of the powders from these groups. Metal powders obtained by the constant and periodically changing regimes of electrolysis are analyzed in detail.

2.2 Silver

2.2.1 Effect of Exchange Current Density on the Morphology of Silver Powder Particles

Electrodeposition of silver from nitrate solutions is characterized by the high exchange current densities, j_0 ($j_0 \gg j_L$, j_L is the limiting diffusion current density) [3, 4] and the typical polarization curve obtained from 0.06 M AgNO$_3$, 1.2 M NaNO$_3$, and 0.05 M HNO$_3$ solution is shown in Fig. 2.1 (denoted by "o"). The plateau of the limiting diffusion current density corresponds to the range of overpotentials between 75 and 175 mV. On the other hand, electrodeposition of silver from ammonium solutions is characterized by the relation $j_0 < j_L$ [4, 5], and the polarization curve for silver electrodeposition obtained from a solution containing 0.1 M AgNO$_3$, 0.5 M (NH$_4$)$_2$SO$_4$, and 0.5 M NH$_3$ is also shown in Fig. 2.1 (denoted by "□"). The plateau of the limiting diffusion current density was
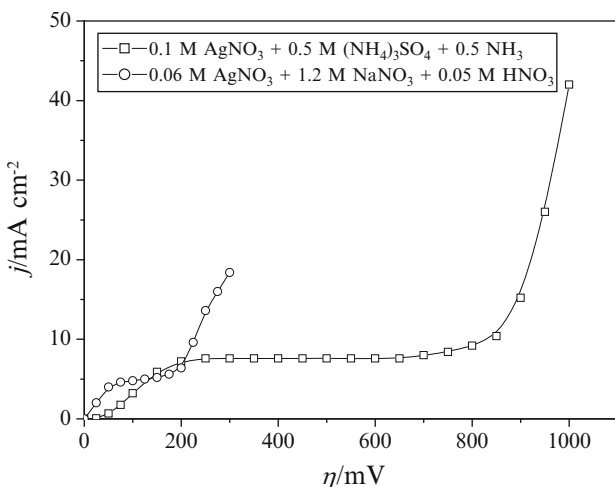
Fig. 2.1 Polarization curves for silver electrodepositions from both 0.1 M $AgNO_3$ + 0.5 M $(NH_4)_2SO_4$ + 0.5 M NH_3 and 0.06 M $AgNO_3$ + 1.2 M $NaNO_3$ + 0.05 M HNO_3 (Reprinted from [4] with permission from Electrochemical Society.)

considerably wider, corresponding to the range of overpotentials between 250 and 700 mV. For both the examined solutions, electrodeposition of silver was performed at the room temperature using vertical cylindrical graphite electrodes [4]. The processes of silver electrodeposition from these solutions were not accompanied with hydrogen evolution reaction.

Due to the large exchange current density in silver nitrate solutions [3], which is significantly higher than in the case of silver ammonium solution [5], an instantaneous growth of dendrites starts at relatively low overpotential [6]. The silver powder electrodeposited from nitrate electrolyte at an overpotential of 150 mV is shown in Fig. 2.2a. Silver particles obtained by tapping the silver deposit from electrode surface represent a mixture of different morphological forms, as illustrated in Fig. 2.2b–d. Some of the particles had the shape of two-dimensional (2D) dendrites (Fig. 2.2b). The presence of other morphological forms, such as crystals of irregular shape and needle-like particles (Fig. 2.2c, d), was also noticed.
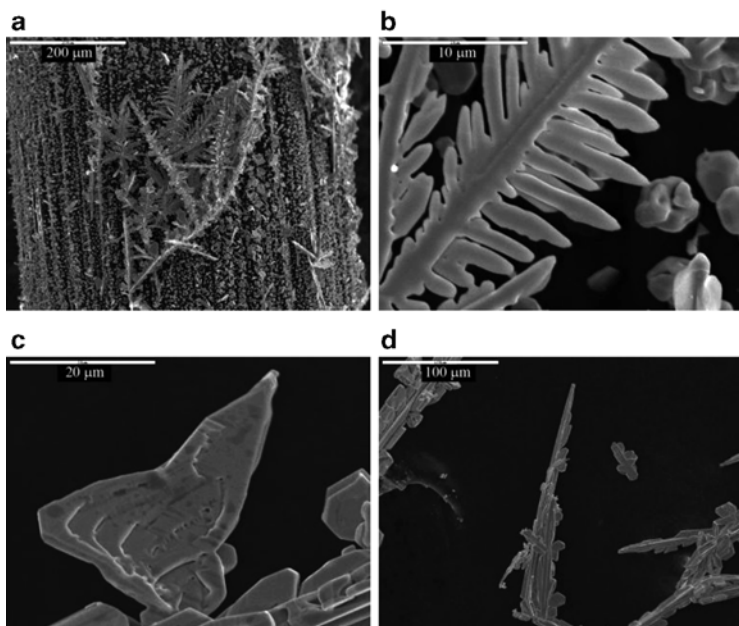
Fig. 2.2 (**a**) Macrostructure and (**b–d**) typical morphological forms of silver obtained by electrodeposition from 0.06 M AgNO$_3$ in both 1.2 M NaNO$_3$ and 0.05 M HNO$_3$ at an overpotential of 150 mV (Reprinted from [4] with permission from Electrochemical Society.)

A typical silver deposit obtained from the ammonium solution at an overpotential of 650 mV is shown in Fig. 2.3a. From Fig. 2.3a, it can be seen that very branchy dendrites are produced at this over-potential. Silver particles obtained by tapping the silver deposit (Fig. 2.3a) are shown in Fig. 2.3b. The dendritic character of this particle is made of the corncob-like elements as presented by the images in Fig. 2.3c, d. A further analysis of the corncob-like elements at the microlevel showed that they are composed of small agg-lomerates of silver grains (Fig. 2.3d). Anyway, morphologies of silver particles electrodeposited from ammonium solution were completely different than those formed during silver electrodeposi-tion from nitrate electrolyte.
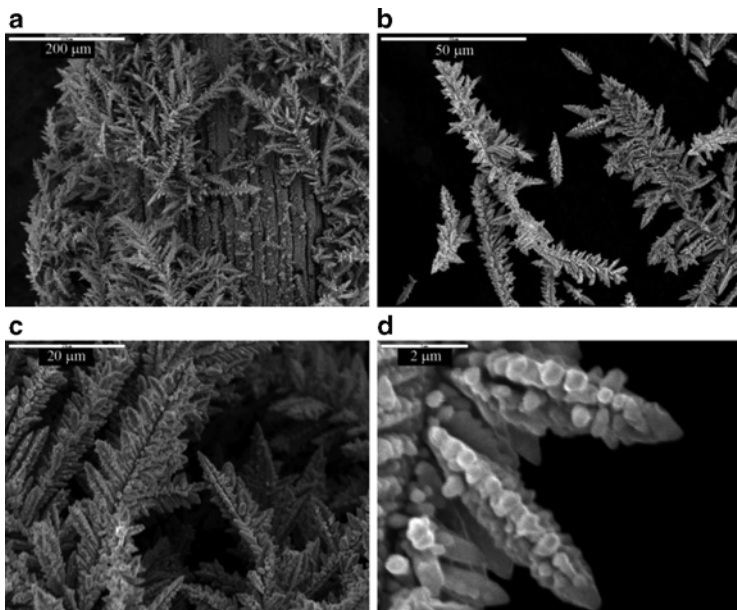
Fig. 2.3 (**a**) Macrostructure of silver powdered deposits electrodeposited at an overpotential of 650 mV from 0.1 M AgNO$_3$ in both 0.5 M (NH$_4$)$_2$SO$_4$ and 0.5 M NH$_3$; (**b**) dendritic particles obtained by tapping this silver deposit; (**c**) and (**d**) the corncob-like elements of which dendrites are composed (Reprinted from [4] with permission from Electrochemical Society.)

It is necessary to note that the shape of the polarization curve for silver electrodeposition from ammonium solution (Fig. 2.1) and morphologies of silver particles (Fig. 2.3) were very similar to those obtained by copper electrodeposition from sulfate solutions at overpotentials corresponding to the plateaus of the limiting diffusion current density [4, 7–11] (see also other chapters). The similarity of silver and copper dendrites was observed at both macro- and microlevels, because both copper and silver dendrites were composed of corncob-like forms, while the corncob-like forms were built of small agglomerates of metal grains [4].

Also, the sudden increase of the current density with the increasing overpotential above 700 mV is the common characteristic of
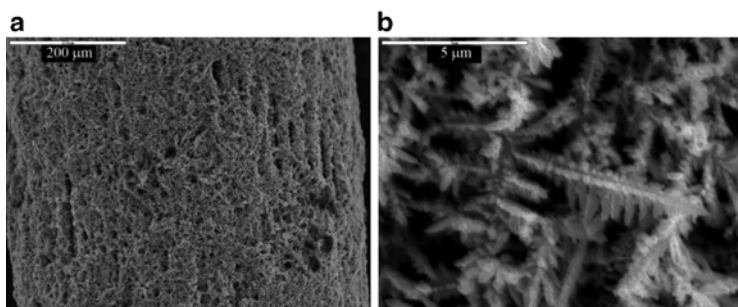
Fig. 2.4 (**a**) Macrostructure of silver powdered deposits electrodeposited at an overpotential of 1,000 mV from 0.1 M $AgNO_3$ in both 0.5 M $(NH_4)_2SO_4$ and 0.5 M NH_3 and (**b**) dendritic particles obtained by tapping silver deposit (Reprinted from [4] with permission from Electrochemical Society.)

both copper electrodeposition from sulfate solution and silver electrodeposition from ammonium solution. Silver powdered deposit obtained from the ammonium solution at an overpotential of 1,000 mV is shown in Fig. 2.4a. At the first sight, spongy-like structure can be noticed from this figure. An analysis of silver deposit produced at the overpotential of 1,000 mV with a higher magnification (Fig. 2.4b) showed that this material is dendritic in shape. Hence, the macrostructure of silver powder formed at an overpotential of 1,000 mV is similar to that of copper and silver deposited at 650 mV. The only difference is in the size of dendrites; silver dendrites electrodeposited at an overpotential of 1,000 mV were considerably smaller than those formed at overpotential of 650 mV, which is attributed to higher nucleation rate at 1,000 mV than at 650 mV [4].

Meanwhile, the macrostructure of the silver deposit produced at an overpotential of 1,000 mV was completely different than that of the copper electrodeposited at the same overpotential. As already mentioned, holes formed by attached hydrogen bubbles surrounded by cauliflower-like agglomerates of copper grains (the honeycomb-like structure; see other chapters) were formed by copper electrode-position at an overpotential of 1,000 mV [7, 8, 10–13]. The copper powder obtained by tapping the powdered deposit consists of an aggregate of small cauliflower-like particles [14]. Similar copper structures were also observed by electrodeposition at periodically changing rate [15–20].

The observed difference in the morphology of silver and copper deposits produced at an overpotential of 1,000 mV can be ascribed to the simultaneous hydrogen evolution reaction during copper electrodeposition at high overpotentials. In the case of copper, hydrogen evolution commences at some overpotential belonging to the plateau of the limiting diffusion current density, and the increasing overpotential intensifies this reaction [7, 11]. At some overpotential outside the plateau of the limiting diffusion current density, hydrogen evolution becomes vigorous enough to cause a strong stirring of the solution leading to a change of the hydrodynamic conditions in the near-electrode layer. Copper dendrites were formed without and with the quantity of evolved hydrogen which was insufficient to lead to the change of hydrodynamic conditions in the near-electrode layer, while cauliflower-like particles (formed around holes) were obtained with the quantity of evolved hydrogen which was enough to lead to the change of the hydrodynamic conditions in the near-electrode layer [7, 11]. The growth of the current with the increasing overpotential was just a result of parallel hydrogen evolution reaction to copper electrodeposition.

In the case of silver, there is no hydrogen evolution, and the increase in the current with the rising overpotential above 700 mV can be ascribed to the instantaneous dendrite growth. The absence of hydrogen evolution during silver electrodeposition is explained by the fact that the equilibrium potential of silver electrode in silver ammonium solution is slightly more positive than the one of copper electrode in copper sulfate solution [21]. On the other hand, it is well known that the hydrogen evolution reaction on copper electrode is somewhat faster than on silver electrode [22]. Consequently, hydrogen evolution does not occur on silver electrode even at an overpotential of 1,000 mV vs. Ag reference electrode.

2.2.2 Effect of Regime of Pulsating Overpotential on the Shape of Silver Powder Particles

Typical deposits obtained in electrodeposition by constant overpotential are shown in Fig. 2.5. Disperse or irregular deposits
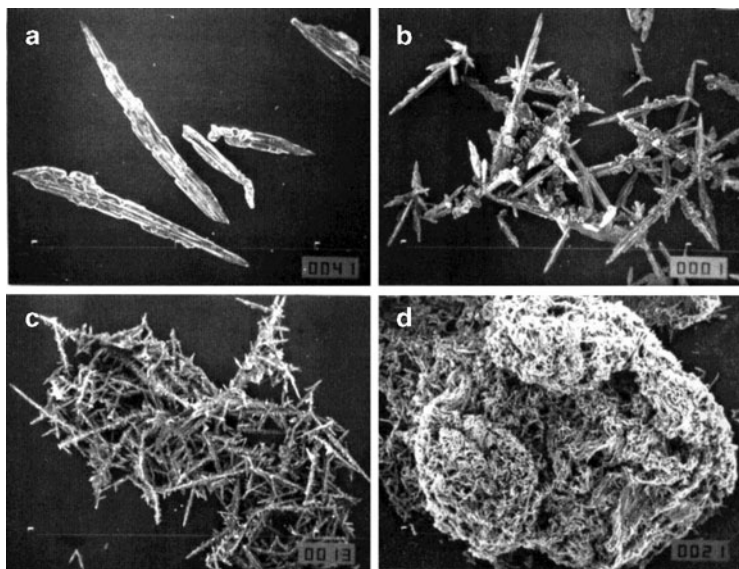
Fig. 2.5 Disperse electrodeposits of silver obtained in constant overpotential deposition at different overpotentials: (**a**) 50 mV, magnification: ×50; (**b**) 100 mV; (**c**) 150 mV; and (**d**) 200 mV; Magnification: ×100 (Reprinted from [23] with permission from the Serbian Chemical Society.)

were obtained at all overpotentials used. In this section, all presented morphologies of silver particles were obtained by electrodepositions from solution containing 0.06 M $AgNO_3$ and 1.2 M $NaNO_3$ in 0.05 M HNO_3 at the room temperature using platinum as the working electrode [23].

Single, nonbranched dendrites were obtained at 50 mV (Fig. 2.5a). Dendrites obtained at 100 mV were occasionally branched (Fig. 2.5b), and some interweaving of the growing dendrites started producing spongy-like agglomerates at 150 mV (Fig. 2.5c). The spongy-like agglomerates obtained at an overpotential of 200 mV were also dendritic, but dendrites are more than ten times shorter than those obtained at lower overpotentials (Fig. 2.6).

The shape of powder particles strongly depends on the type of working electrode used [23]. Agglomeration of silver powder
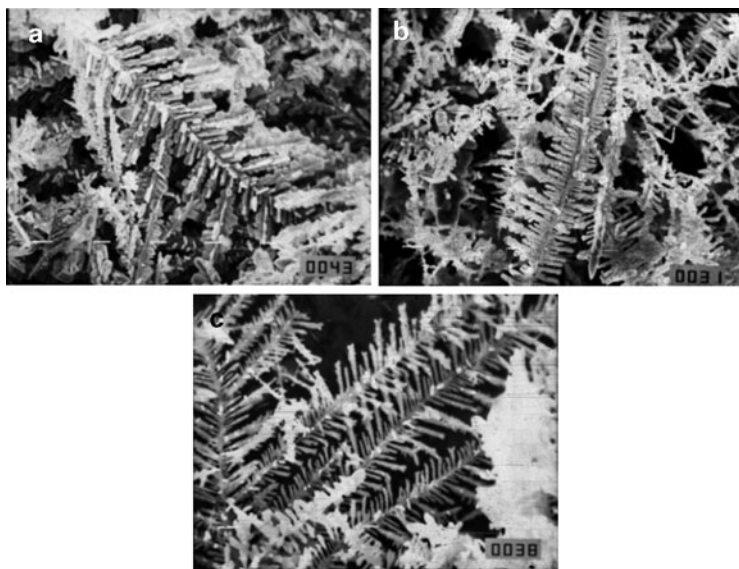
Fig. 2.6 Same as in Fig. 2.5 but (**a**) 200 mV, ×2000; (**b**) 250 mV, ×3500; and (**c**) 300 mV, ×5000 (Reprinted from [23] with permission from the Serbian Chemical Society and copied by permission from the "Electrochemistry Encyclopedia" (http://electrochem.cwru.edu/ed/encycl/) on 04/25/2007. The original material is subject to periodical changes and updates.)

particles was not observed when electrodeposition of silver was performed from the same solution in the overpotential range between 140 and 200 mV onto graphite electrodes [24].

The elimination of agglomerates of powder particles obtained at high overpotentials and the formation of single particles can be realized by treating the powder in an ultrasonic bath [23]. Figure 2.7a shows the single particles obtained by destroying the agglomerates obtained at an overpotential of 200 mV (Fig. 2.5d) in an ultrasonic bath. The detail from Fig. 2.7a is shown in Fig. 2.7b. A similar situation was observed with powder agglomerates formed at over-potentials of 250 and 300 mV [23].

The prevention of formation of agglomerates of particles and the formation of individual particles can be realized by the application of periodically changing regimes of electrolysis [23]. This can be
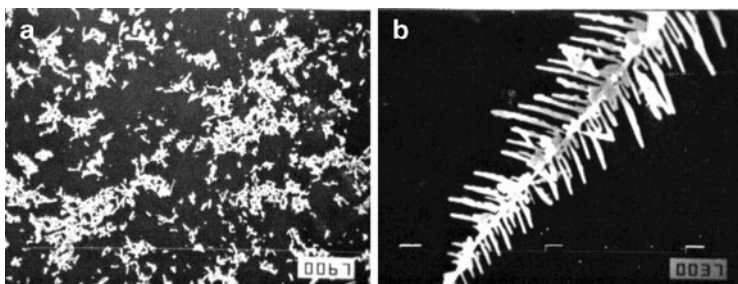
Fig. 2.7 (**a**) Same as in Fig. 2.5d but after treatment in ultrasonic bath: ×100 and (**b**) detail from Fig. 2.7a; ×5000 (Reprinted from [23] with permission from the Serbian Chemical Society.)

explained by the fact that the reversible potential of a surface with a radius of curvature r would depart from that of a planar surface by the quantity [25]:

$$\Delta E = \frac{2\sigma V}{Fr}, \tag{2.1}$$

where σ is the interfacial energy between the metal and solution, F is the Faraday constant, V is the molar volume, and r is the protrusion tip radius. For example, this makes the equilibrium potential of spongy zinc deposits 7–10 mV more cathodic than that of zinc foil [26–28]. Obviously, the tips of dendrites characterized by small tip radii will dissolve faster than the flat surface in electrodeposition by all current or overpotential waveforms that are characterized by some anodic current flow [26–30]. In this way, the branching of dendrites is decreased and powder particles become less dendritic and more compact.

Typical deposits obtained by square-wave pulsating overpotential (PO) are shown in Figs. 2.8–2.10. It can be noticed by the analysis of these figures the decrease of both agglomeration and dendritic character of powder particles with the increasing "off" period and decreasing overpotential amplitude.

This effect was quantitatively discussed for the regime of the square-wave pulsating overpotential [23, 31].
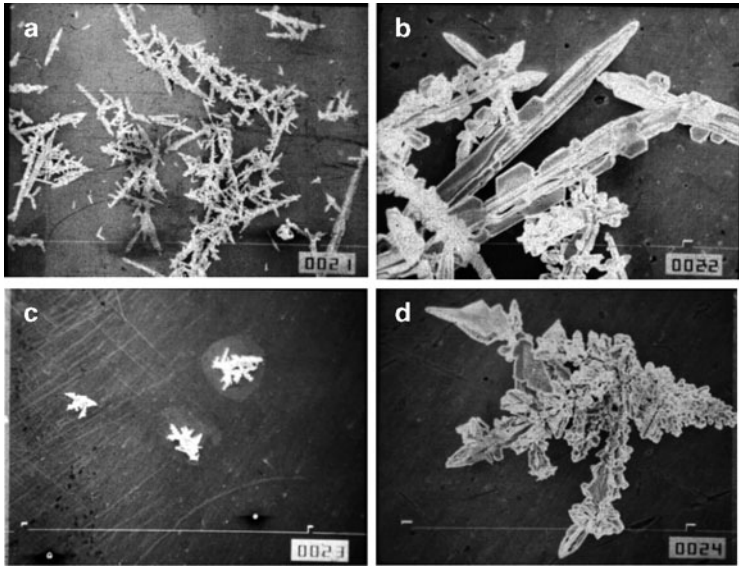
Fig. 2.8 Silver powder particles obtained by square-wave pulsating overpotential. Overpotential amplitude: 300 mV. Pulse duration: 5 ms. (**a**) Pause to pulse ratio: 1, ×100; (**b**) pause to pulse ratio: 1, ×1000; (**c**) pause to pulse ratio: 3, ×100; and (**d**) pause to pulse ratio: 3, ×1000 (Reprinted from [23] with permission from the Serbian Chemical Society.)

Square-wave pulsating overpotential is described by [23, 32]

$$\frac{\partial C}{\partial t} = D \frac{\partial^2 C}{\partial x^2}, \tag{2.2}$$

$$C(x, 0) = C_0, \tag{2.3}$$

$$C(\delta, t) = C_0, \tag{2.4}$$

$$\frac{\partial C(0, t)}{\partial x} = \frac{j_0}{nFD} \left[\frac{C(0, t)}{C_0} \exp\left(\frac{2.3\eta}{b_c}\right) - \exp\left(-\frac{2.3\eta}{b_a}\right) \right], \tag{2.5}$$
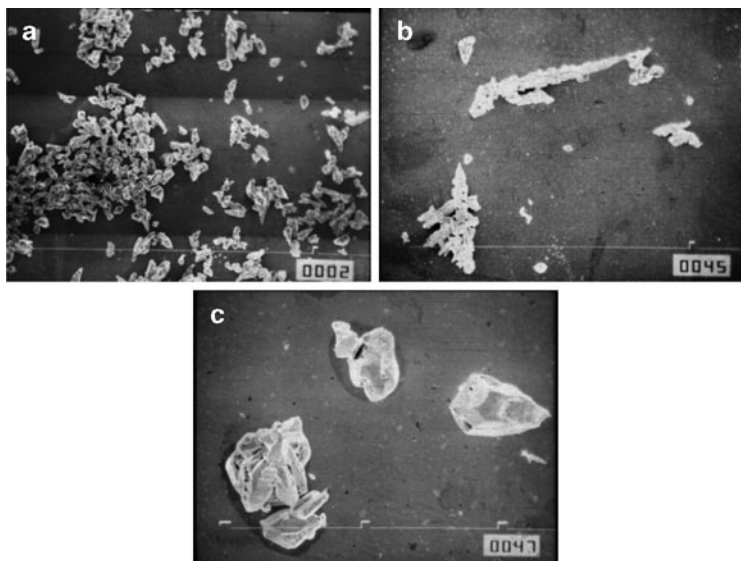
Fig. 2.9 Same as in Fig. 2.8. Overpotential amplitude: 100 mV. Pulse duration: 0.5 s. Pause to pulse ratio: 1: (**a**) ×100, (**b**) ×100; and (**c**) ×500 (Reprinted from [23] with permission from the Serbian Chemical Society.)

where j_0 is the exchange current density, n is the number of transferred electrons, D is the diffusion coefficient, b_c and b_a are the cathodic and anodic Tafel slopes, η is the overpotential, C is the concentration, C_0 is the bulk concentration, t is the time, and x is the coordinate in horizontal direction. η is given by

$$\eta = \begin{cases} \eta_A & \text{for} \quad mT_p < t \le \left(m + \dfrac{1}{p+1}\right)T_p \\ 0 & \text{for} \quad \left(m + \dfrac{1}{p+1}\right)T_p < t \le (m+1)T_p \end{cases} \qquad (2.6)$$

$$m = 0, 1, 2, \ldots,$$

where η_A is the overpotential amplitude, T_p is the period of pulsation, and p is the pause to pulse ratio.
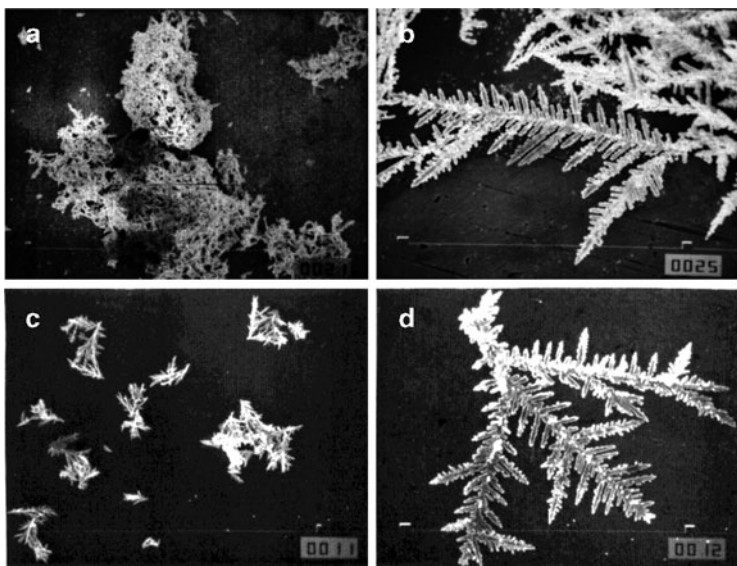
Fig. 2.10 Same as in Fig. 2.8. Overpotential amplitude: 250 mV. Pulse duration: 0.5 s. (**a**) Pause to pulse ratio: 1, ×100; (**b**) pause to pulse ratio: 1, ×1000; (**c**) pause to pulse ratio: 2, ×100; and (**d**) pause to pulse ratio: 2, ×1000 (Reprinted from [23] with permission from the Serbian Chemical Society.)

Assuming that the surface concentration in pulsating overpotential deposition does not vary with time, at sufficiently high frequencies it is easy to show the response of the current density, j, to the input overpotential:

$$
j =
\begin{cases}
j_0\left(1 - \dfrac{j_{av}}{j_L}\right)\exp\left(\dfrac{2.3\eta_A}{b_c}\right) - j_0\exp\left(-\dfrac{2.3\eta_A}{b_a}\right) \\
\qquad\qquad \text{for} \quad mT_p < t \leq \left(m + \dfrac{1}{p+1}\right)T_p \ \text{(a)} \\
-j_{av}\dfrac{j_0}{j_L} \quad \text{for} \quad \left(m + \dfrac{1}{p+1}\right)T_p < t \leq (m+1)T_p \ \text{(b)}
\end{cases}
\tag{2.7}
$$

where j_{av} is the average current density and j_L is the limiting diffusion current density.

Equations (2.2)–(2.7) are valid for the flat electrode surfaces or protrusions with sufficiently large tip radii where the surface energy

term [25] can be neglected. If it cannot be neglected, then the surface energy term affects the reaction rate [33], and for one electron transfer process, it is valid Eq. (2.8):

$$\frac{\partial C}{\partial x} = \frac{j_0}{nFD} \left[\left(1 - \frac{j_{av}}{j_L} \right) \exp\left(-\frac{2\beta\sigma V}{RTr} \right) \exp\left(\frac{2.3\eta}{b_c} \right) \right.$$
$$\left. - \exp\left(\frac{2(1-\beta)\sigma V}{RTr} \right) \exp\left(-\frac{2.3\eta}{b_a} \right) \right], \qquad (2.8)$$

where β is a symmetry factor, T is the temperature and R is the gas constant.

The right-hand side of Eq. (2.5) should be transformed by taking Eq. (2.8) into account. The output current during pauses ($\eta = 0$) becomes

$$j = -j_0 \exp\left(\frac{2(1-\beta)\sigma V}{RTr} \right), \qquad (2.9)$$

if $r \to 0$.

It is easy to show that the difference between the current density on the flat surface and at the tip of the dendrites during the "off" period:

$$\Delta j = j_0 - j_0 \exp\left(\frac{2(1-\beta)\sigma V}{RTr} \right), \qquad (2.10)$$

if $j_{av} \approx j_L$, which leads to

$$h = h_0 + \frac{V j_0}{F} \left[1 - \exp\left(\frac{2(1-\beta)\sigma V}{RTr} \right) \right] t \qquad (2.11)$$

because of

$$\frac{dh}{dt} = \frac{V \Delta j}{F}, \qquad (2.12)$$

where h is the height of protrusion and h_0 is the initial height of protrusion, and taking Eq. (2.10) into account,

$$\frac{\mathrm{d}h}{\mathrm{d}t} = \frac{Vj_0}{F}\left[1 - \exp\left(\frac{2(1-\beta)\sigma V}{RTr}\right)\right]. \tag{2.13}$$

Equation (2.11) represents the change of the height of the protrusion with tip radius r relative to the flat surface or the protrusion with sufficiently large r. In square-wave PO electrodeposition [29, 34], the filaments on the growing grains formed in spongy electrodeposition can be completely dissolved during the pause leading to the formation of compact deposit. In powder electrodeposition by the same regime, the dissolution of branches on the dendrite stalk is also expected.

Hence, the larger the "off" period, the less dendritic particles are obtained. On the other hand, the current density during the "on" period on the tip of dendrites growing inside the diffusion layer is given by:

$$j = j_0 \frac{h}{\delta} \exp\left(\frac{2.3\eta_{\mathrm{A}}}{b_{\mathrm{c}}}\right), \tag{2.14}$$

which is a somewhat modified Eq. (2.7) [35], where δ is the thickness of diffusion layer. For the same "on" period the particles will be more dendritic with increasing overpotential amplitude. In the millisecond range the ratio between the overpotential corresponding to bulk diffusion control and the activation overpotential can be reduced to the value corresponding to electrodeposition at lower overpotentials in the constant overpotential regime. Hence, deposits obtained in the PO regimes (at the same η_{A} and with different p used) are more similar to those obtained in the constant overpotential regime ($p = 0$) at lower overpotentials than the one corresponding to η_{A} in the PO regimes. The degree of diffusion control decreases with increasing p, even at the limiting diffusion current density, and it can become sufficient to produce the quality of deposits corresponding to mixed, activation, or surface energy control. This will be discussed in more detail in the case of lead electrodeposition.

The above discussion well explains the morphologies of silver deposits obtained in the millisecond range (Fig. 2.8), as well as to some extent in the second range (Figs. 2.9 and 2.10). In the latter case, the anodic current decreases during the "off" period, and this effect is also observed in electrodeposition by the regime of pulsating current (PC). In these cases, the dissolution of disperse metal occurs by the mechanism of galvanic microcells at the higher pause to pulse ratios [36–39]. Obviously, the agglomerate formation cannot be completely prevented in this way except at very low overpotential amplitude.

The second effect of the application of periodically changing regimes of electrolysis on the morphology of powder particles is that the metal adatoms on the surface, which are not in stable positions, dissolve easier than the atoms from the crystal lattice, permitting the formation of ideal crystal planes on powder particles. Powder particles of silver obtained by pulsating and polarity-reversing techniques are almost small monocrystals [1, 24].

2.3   Lead

Electrodeposition of lead belongs to the fast electrochemical processes because it is characterized by a large exchange current density, j_0 [40]. Figure 2.11 shows the polarization curve for lead electrodeposition from solution containing 0.50 M $Pb(NO_3)_2$ in 2.0 M $NaNO_3$. All experiments presented here were performed at the room temperature using cylindrical copper wires as the working electrodes [41]. The reference and counter electrodes were of a pure lead. The polarization curve obtained from this solution consisted of two parts. The characteristic of the first part is linear dependence of the current density on the overpotential. After an overpotential of about 100 mV, the current density increased quickly, and this rapid increase of the current with the overpotential is the characteristic of the second part of the polarization curve.

The linear dependence of the current density on overpotential corresponds to ohmic-controlled electrodeposition [42, 43]. The mechanism of the ohmic-controlled electrodeposition of metals is presented
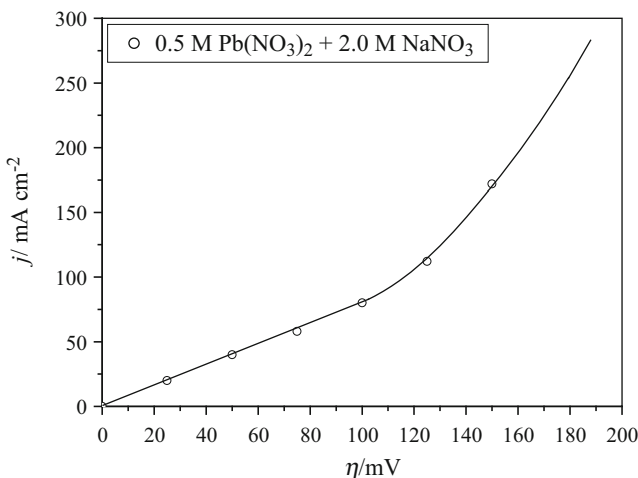
Fig. 2.11 Polarization curve for lead electrodeposition from 0.50 M Pb(NO$_3$)$_2$ in 2.0 M NaNO$_3$

in Chap. 1. As already mentioned, for sufficiently fast electrode processes ($j_0/j_L \geq 100$), there is no activation or diffusion polarization before the limiting diffusion current density is reached. At current densities lower than the limiting diffusion ones, the measured overpotential is due to the ohmic voltage drop between the electrode and the tip of Lugin capillary [44]. When the limiting diffusion current density is reached, the process of electrochemical deposition is under complete diffusion control. Meanwhile, as seen from Fig. 2.11, instead of the plateau of the limiting current density the inflection point on the polarization curve was observed. This inflection point on the polarization curve corresponds to an overpotential of about 100 mV. The survey of lead surface morphologies obtained at different overpotentials was the most suitable way to analyze this polarization curve and hence the lead electrodeposition system.

Figures 2.12–2.14 show morphologies of lead deposits obtained in the ohmic-controlled deposition (Fig. 2.12), in the transitional zone corresponding to the end of the ohmic-controlled electrodeposition (Fig. 2.13) and to the zone of rapid increase of the current of electrodeposition (Fig. 2.14).
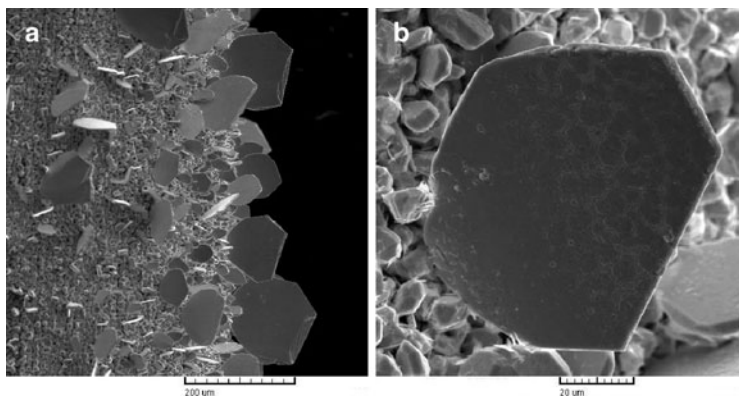
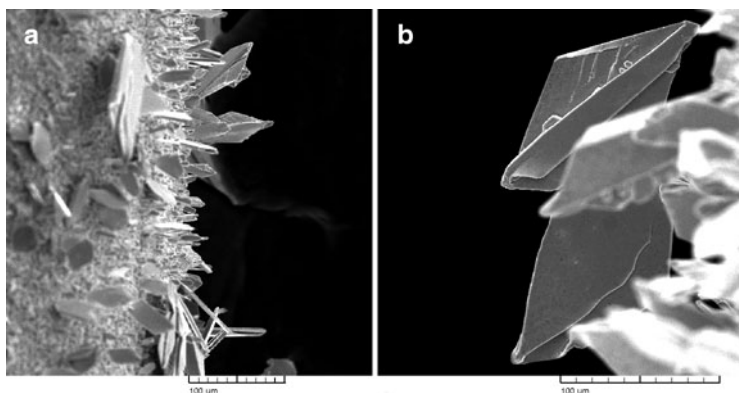**Fig. 2.12** Lead deposits obtained at an overpotential of 50 mV. Time of electrolysis: 180 s

Fig. 2.13 Lead deposits obtained at an overpotential of 100 mV. Time of electrolysis: 60 s

The single lead crystals were obtained in ohmic-controlled electrodeposition at an overpotential of 50 mV (Fig. 2.12). The formation of these single crystals was accompanied by a slight increase in the current during the electrodeposition process. Figure 2.13 shows that the mixture of different regular geometric forms from single crystals to those given in Fig. 2.13b was obtained at an overpotential of 100 mV
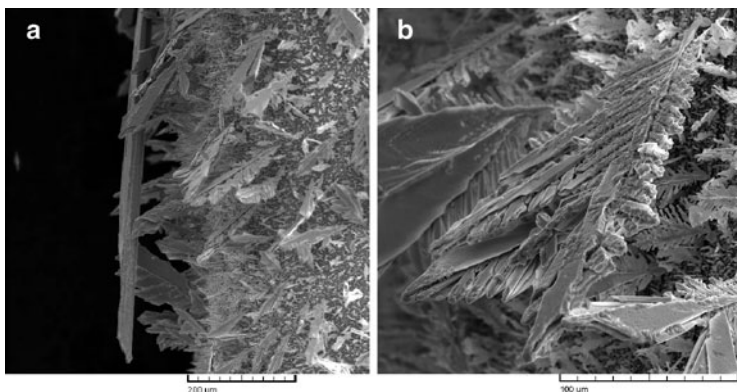
Fig. 2.14 Lead deposits obtained at an overpotential of 150 mV. Time of electrolysis: 20 s

corresponding to the inflection point. The formation of these morphological forms was accompanied by an increase in the current of electrodeposition of about 50% in relation to the initial current of electrodeposition. Finally, the increase of the current during electrodeposition processes at overpotentials higher than 100 mV was very quick and the morphology of electrodeposited lead obtained at an overpotential of 150 mV after double increase of current in relation to the initial electrodeposition current is shown in Fig. 2.14. From Fig. 2.14, it can be clearly seen that the single and two-dimensional (2D) lead dendrites were dominant morphological forms obtained at this overpotential (Fig. 2.14).

To better clarify the formed morphological forms (especially those obtained at an overpotential of 100 mV), these lead deposits were compared with those obtained in the galvanostatic regime. In the galvanostatic regime, lead electrodeposition was performed at current densities of 100 and 160 mA/cm^2. These current densities corresponded to the final currents during electrodeposition in the potentiostatic regime of electrolysis at overpotentials of 100 and 150 mV, respectively. Figures 2.15 and 2.16 show lead deposits obtained at current densities of 100 mA/cm^2 (Fig. 2.15) and 160 mA/cm^2 (Fig. 2.16). The single and 2D (two-dimensional) dendrites were the dominant morphological forms obtained at the
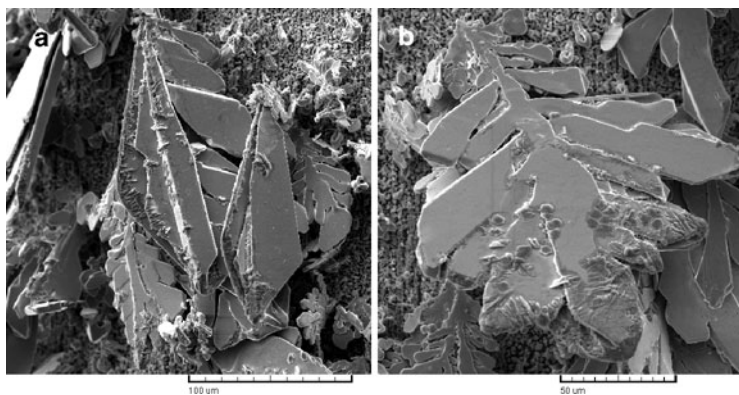
Fig. 2.15 Lead deposits obtained at a current density of 100 mA/cm^2. Time of electrolysis: 60 s
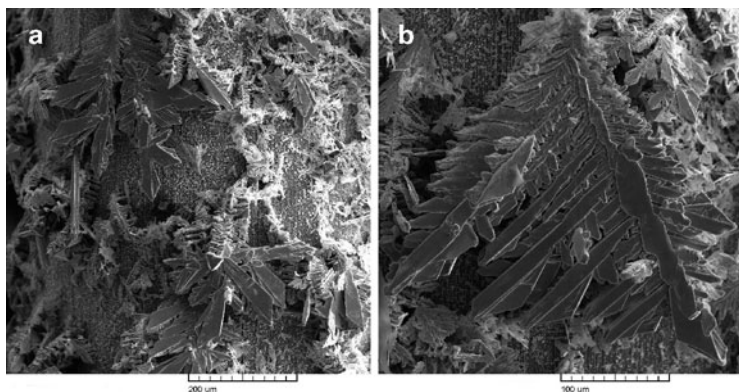

Fig. 2.16 Lead deposits obtained at a current density of 160 mA/cm^2. Time of electrolysis: 20 s

both current densities. The shape of 2D dendrites obtained at a current density of 100 mA/cm^2 clearly indicates that the regular geometric forms obtained at an overpotential of 100 mV (Fig. 2.13b) represents the precursors of dendrites.

It is necessary to note that dendrites obtained in the galvanostatic regime were more branchy structures than those obtained in the

potentiostatic regime. One of the reasons for it is the fact that during electrodeposition in the galvanostatic regime at the current density of 160 mA/cm^2, the initial overpotential was about 220 mV, and the overpotential of about 110 mV was attained after electrodeposition with an electrolysis time of 20 s. A similar situation was also observed during lead electrodeposition at 100 mA/cm^2.

The shape of lead dendrites falls under the classical Wranglen's definition of a dendrite. According to Wranglen [45], dendrites consist of stalk and primary and secondary branches. From Figs. 2.14–2.16, these elements of dendrites are clearly visible. From the electrochemical point of view, a dendrite is defined as an electrode surface protrusion that grows under activation control, while electrodeposition to the macroelectrode is predominantly under diffusion control [6, 33, 46, 47]. For very fast electrodeposition processes, the critical overpotential for dendritic growth initiation, η_I, and the critical overpotential for instantaneous dendritic growth, η_c, depend on the metal surface energy and they are of the order of a few millivolts [6]. The initiation of the dendritic growth is followed by the strong increase of the apparent current density because the current density on the tips of formed dendrites is under mixed activation–diffusion or complete activation control. Hence, the strong increase of current with overpotentials higher than 100 mV corresponds to the activation-controlled electrodeposition on the tips of formed dendrites. On the other hand, the inflection point estimated to be at an overpotential of 100 mV corresponds to the transition between ohmic and activation-controlled electrodeposition process.

The two-dimensional forms were only obtained during lead electrodeposition. The two-dimensional nucleation was also a characteristic of silver electrodeposition from nitrate solution (Fig. 2.2) [4]. The polarization curve with an inflection point was also obtained in the case of silver electrodeposition from nitrate solution when the strong increase of current density was accompanied by the formation of dendrites [42, 43]. The common characteristic of these metal electrodeposition processes is affiliation to the same group of metals, i.e., to group of normal metals [Cd, Zn, Pb, Sn, Ag (silver nitrate solutions)] [2] which are characterized by a low melting point, T_m, and high exchange current density, j_0. This indicates a strong relationship between nucleation type and the type of metal.
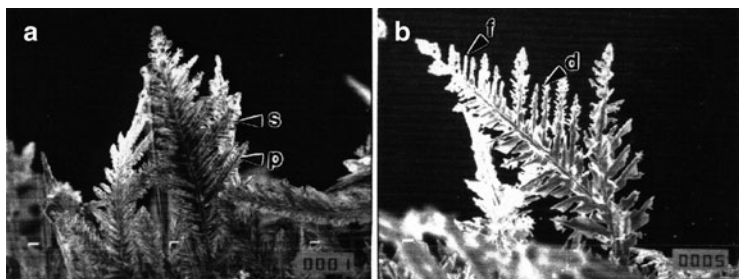
Fig. 2.17 Lead deposit obtained at constant overpotential deposition: (**a**) after 50 s at 75 mV, magnification: ×500 and (**b**) the same as in (**a**) but after 350 s at 0 mV, magnification: ×750 (Reprinted from [48] with permission from Elsevier and [6] with permission from Springer.)

2.3.1   The Effect of the Regime of Pulsating Overpotential on Morphology of Powder Particles

Figure 2.17a shows the lead dendrite obtained in the constant potentiostatic regime at an overpotential of 75 mV with an electrolysis time of 50 s. In all experiments for which results are presented in this section, the processes of electrodeposition were performed from solution containing 0.1 M Pb(CH$_3$COO)$_2$, 1.5 M NaCH$_3$COO, and 0.15 M CH$_3$COOH [48]. The other experimental conditions were same as for the previously analyzed solution. It is clearly visible that this dendrite possesses well-developed primary and secondary (indicated by S in Fig. 2.17a) dendrite arms as well as sharp crystallographic morphology. Figure 2.17b shows dendrites formed under the same conditions as those shown in Fig. 2.17a but obtained after a treatment at an overpotential of 0 mV with a time of 350 s. The dissolution of secondary dendrite arms occurs due to the difference in equilibrium potential between points with the different radii of curvature and the degree of dissolution varies from full dissolution (indicated by F in Fig. 2.17b) to the presence of
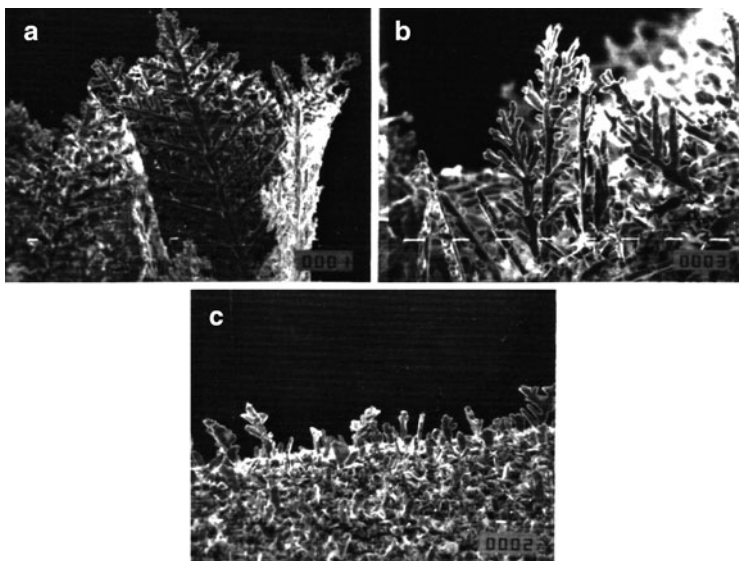
Fig. 2.18 Lead deposit obtained by square-wave pulsating overpotential at an overpotential amplitude of 75 mV with a pulse duration of 5 s and a deposition time of 120 s: (**a**) pause-to-pulse ratio: 1, ×500; (**b**) pause-to-pulse ratio: 3, ×1500, and (**c**) pause-to-pulse ratio 5, ×1000 (Reprinted from [48] with permission from Elsevier.)

secondary arm debris (indicated by D in Fig. 2.17b). Selective dissolution of dendrite arms during the "off" period due to their different tip radii is also seen from Figs. 2.18–2.20. So, increasing the pause-to-pulse ratio p enhanced the formation of more compact and less branched particles.

In addition to dissolution of dendrites, another phenomenon is observed. The sharp crystallographic forms (Figs. 2.18a, 2.19a, 2.20a, c) are absent with increasing p. Also, the sharp crystallographic edges present in the deposited dendrites become partially or well rounded after dissolution.

Of course, the formation of more compact and less branchy powder particles in the PO electrodepositions with the increasing p (at the one and the same η_A) can be ascribed to the fact that
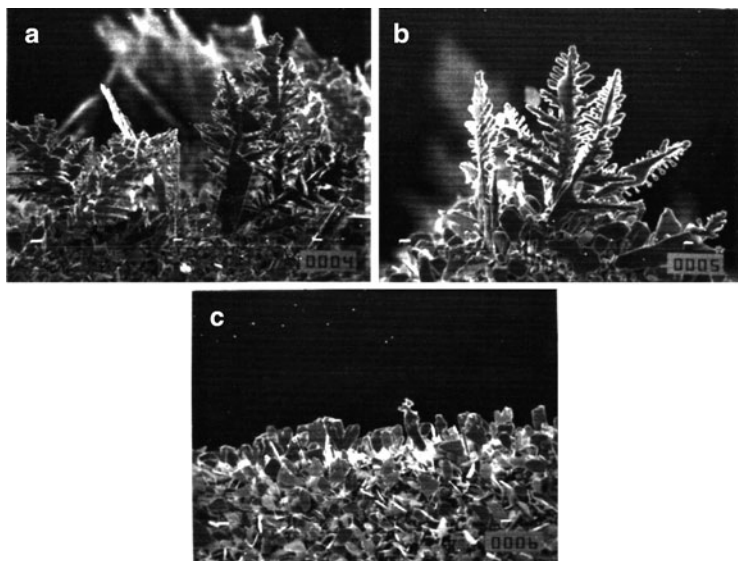
Fig. 2.19 Lead deposit obtained by square-wave pulsating overpotential at an overpotential amplitude of 75 mV with a pulse duration of 0.5 s and a deposition time of 120 s: (**a**) pause-to-pulse ratio: 1, ×500; (**b**) pause-to-pulse ratio: 3, ×1000, and (**c**) pause-to-pulse ratio: 5, ×1000 (Reprinted from [48] with permission from Elsevier and [6] with permission from Springer.)

particles with lower tip radii are dissolved faster than those with larger ones [25]. This selective dissolution is a result of the anodic current density during "off" periods, and although this current density can be neglected in relation to the cathodic one during "on" periods, its effect on the morphology of powder particles is very high. Aside from already observed the effect of the anodic current density on the morphology of silver particles, this effect was also observed during the formation of powder particles of some other metals, such as Sn [35].

This phenomenon can be qualitatively treated and Eqs. (2.2)–(2.7) are also valid for this case. Equations (2.2)–(2.7) are valid for flat electrode surfaces or protrusions with sufficiently large tip radii, where the surface energy term [25] can be neglected. If it cannot be
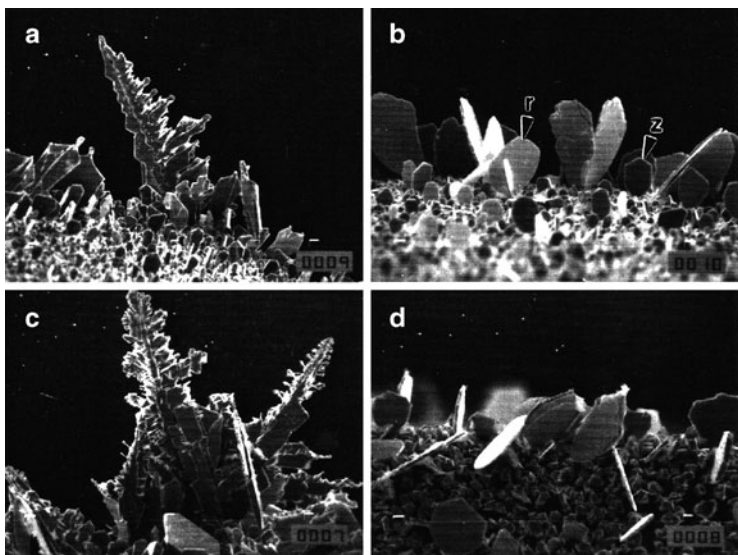
Fig. 2.20 Lead deposit obtained by square-wave pulsating overpotential at an overpotential amplitude of 75 mV with a deposition time of 120 s: (**a**) pulse duration: 0.05 s, pause-to-pulse ratio: 1, ×500; (**b**) pulse duration: 0.05 s, pause-to-pulse ratio: 3, ×1000; (**c**) pulse duration: 0.1 ms, pause-to-pulse ratio: 1, ×500; and (**d**) pulse duration 0.1 ms, pause-to-pulse ratio: 3, ×1000 (Reprinted from [48] with permission from Elsevier.)

neglected, the effect of the surface energy term on the reaction rate [33] for two electron reaction steps is described by Eq. (2.15) [31]:

$$\frac{\partial C(0,t)}{\partial x} = \frac{j_0}{nFD}\left[\left(1 - \frac{j_{av}}{j_L}\right)\exp\left(\frac{2.3\eta}{b_c}\right) - \exp\left(\frac{2\sigma V}{RTr}\right)\exp\left(-\frac{2.3\eta}{b_a}\right)\right].$$

(2.15)

The output current density, j, during pauses ($\eta = 0$) at the tip of the dendrite is presented by Eq. (2.16):

$$j = j_0\left(1 - \frac{j_{av}}{j_L}\right) - j_0\exp\left(\frac{2\sigma V}{RTr}\right).$$

(2.16)

The corresponding output current density on the flat surface is given by Eq. (2.7b). The difference between the current density at the tip of the dendrite and on the flat surface during the "off" period is given by Eq. (2.17):

$$\Delta j = j_0 - j_0 \exp\left(\frac{2\sigma V}{RTr}\right), \tag{2.17}$$

if $j_{av} \approx j_L$, which is satisfied in most cases of dendrite growth.

Then, the change of height of surface protrusions with tip radius r relative to the flat surface is given by Eq. (2.18) [34]:

$$\frac{dh}{dt} = \frac{V\Delta j}{nF}, \tag{2.18}$$

and finally, for the two electron reaction steps:

$$h = h_0 + \frac{Vj_0}{2F}\left[1 - \exp\left(\frac{2\sigma V}{RTr}\right)\right]t, \tag{2.19}$$

where

$$\left(m + \frac{1}{p+1}\right)T_p < t \leq (m+1)T_p. \tag{2.20}$$

Equation (2.19) represents the height of the dendrite with tip radius r as a function of time, relative to the flat surface or to the protrusion with sufficiently large r. It is obvious that dendrites with very low tip radii can be completely dissolved during the pause. This means that the branching of dendrites can be prevented in square-wave pulsating overpotential deposition. Obviously, the larger p, the greater the degree of dissolution, as follows from Eq. (2.20). The effect is more pronounced if η_A remains constant and p increases, as seen from Figs. 2.18–2.20.

The effect of the "off" period on the micromorphology of metal powder particles can also be seen by the following analysis of lead surface morphology. The lead dendrites obtained in the PO
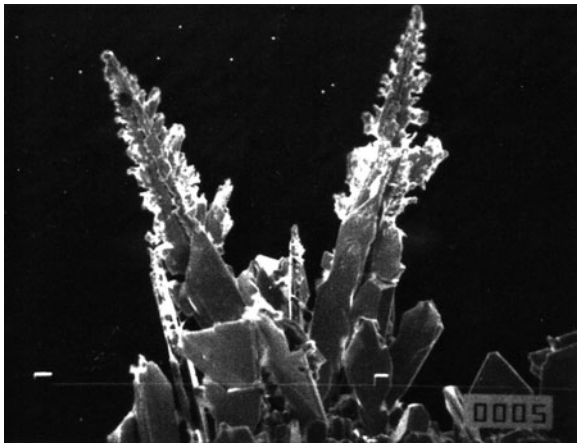
Fig. 2.21 Lead deposit obtained in constant overpotential deposition at 30 mV with a deposition time of 120 s. Magnification: ×750 (Reprinted from [48] with permission from Elsevier.)

electrodeposition using overpotential amplitude of 75 mV and $p = 1$ at frequencies of 10 and 5,000 Hz (Fig. 2.20a, c) are more similar to those obtained at constant overpotential of 30 mV (Fig. 2.21) than those obtained at 75 mV (Fig. 2.17a), what can be explained as follows.

The average current density in the pulsating overpotential deposition can be obtained from [34]

$$j_{av} = \frac{j_0}{p+1}\left[\left(1 - \frac{j_{av}}{j_L}\right)\exp\left(\frac{2.3\eta_A}{b_c}\right) - p\frac{j_{av}}{j_L}\right], \qquad (2.21)$$

if the anodic current density is neglected during overpotential pulses, and the overpotential amplitude can then be obtained in the form

$$\eta_A = \frac{b_c}{2.3}\ln\frac{j_{av}}{j_0} + \frac{b_c}{2.3}\ln\left(p + 1 + \frac{pj_0}{j_L}\right) + \frac{b_c}{2.3}\ln\left(\frac{1}{1 - j_{av}/j_L}\right). \qquad (2.22)$$

The third term in Eq. (2.22) corresponds to bulk diffusion control. It remains constant for a determined average current density regardless of the pause-to-pulse ratio, whereas the second term, which with the first one represents the activation part of the overpotential, increases with increasing p. In this way the ratio between overpotential corresponding to bulk diffusion control and activation overpotential can be reduced to the value corresponding to the deposition at lower overpotentials in the constant overpotential regime. So, it can be expected that deposits obtained at η_A in pulsating regimes ($p > 0$) are more similar to those obtained at lower overpotentials than at η_A in the constant overpotential regime ($p = 0$).

On the other hand [32], the overpotential and current density on the tips of growing dendrites inside the diffusion layer are related by:

$$j_d = j_0 \frac{h}{\delta} \exp\left(\frac{2.3\eta_A}{b_c}\right) \tag{2.14}$$

and

$$j_{d,av} = j_0 \frac{h}{\delta(p+1)} \exp\left(\frac{2.3\eta_A}{b_c}\right) \tag{2.23}$$

in the constant and pulsating overpotential regimes, respectively. This means that dendritic growth is reduced in pulsating overpotential deposition. This is the second reason why dendrites, or powder particles, obtained in pulsating overpotential deposition are more similar to those obtained at lower overpotentials than to those obtained at overpotential amplitude in constant overpotential deposition.

The effect of the frequency of pulsation on the morphology is also illustrated by Figs. 2.18–2.20. It seems that under deposition at high frequencies (Fig. 2.20) more pronounced anodic dissolution during the pause occurs compared with the deposition at lower frequencies (Figs. 2.18 and 2.19), which leads to a formation of less dendritic deposit.

The difference between the morphologies obtained at lower and higher frequencies can be explained as follows. At sufficiently high frequencies the current response to the input overpotential is given by Eq. (2.7), while at lower frequencies it is given by

$$j = \begin{cases} j_0 \dfrac{C(0,t)}{C_0} \qquad \exp\left(\dfrac{2.3\eta_A}{b_c}\right) - j_0 \exp\left(-\dfrac{2.3\eta_A}{b_a}\right) \\ \qquad\qquad \text{for} \quad mT_p < t \le \left(m + \dfrac{1}{p+1}\right)T_p \qquad \text{(a)} \\ j_0\left(\dfrac{C(0,t)}{C_0} - 1\right) \text{for} \quad \left(m + \dfrac{1}{p+1}\right)T_p < t \le (m+1)T_p \text{ (b)} \end{cases}$$

$$(2.24)$$

The anodic current during the "off" period is constant and can have significant value at sufficiently high frequencies [Eq. (2.7b)]. At lower frequencies [Eq. (2.24b)], when $C(0,t)$ becomes equal to C_0 the anodic current is zero and the average anodic current during the "off" period can be considerably lower than in the previous case.

Hence, the change of morphology of the deposit can be the indicator of the frequency at which the surface concentration becomes independent of time in pulsating overpotential deposition. This happens at a frequency of 10 Hz as seen from Figs. 2.19 and 2.20.

The formation of silver and lead powdered deposits from nitrate solutions was accompanied by the absence of hydrogen evolution as the second reaction. In the case of silver, the reason for it is the fact that the reversible potential of silver electrode is sufficiently positive to avoid hydrogen evolution reaction. In the case of lead, hydrogen evolution is extremely slow process, and then, hydrogen evolution is negligible at overpotentials at which lead was electrodeposited. The extremely high exchange current densities of these metals permit the formation of dendrites at low overpotentials, and very pronounced effect of selective dissolution during the "off" periods in the pulsating overpotential regime in both the millisecond and second range was observed.

2.4 Cadmium

Cadmium also belongs to the group of normal metals which are characterized by the large exchange current densities. In the case of cadmium, hydrogen evolution is also a slow process and this fact enables the analysis of the formation of cadmium dendrites without the effect of any parallel process.
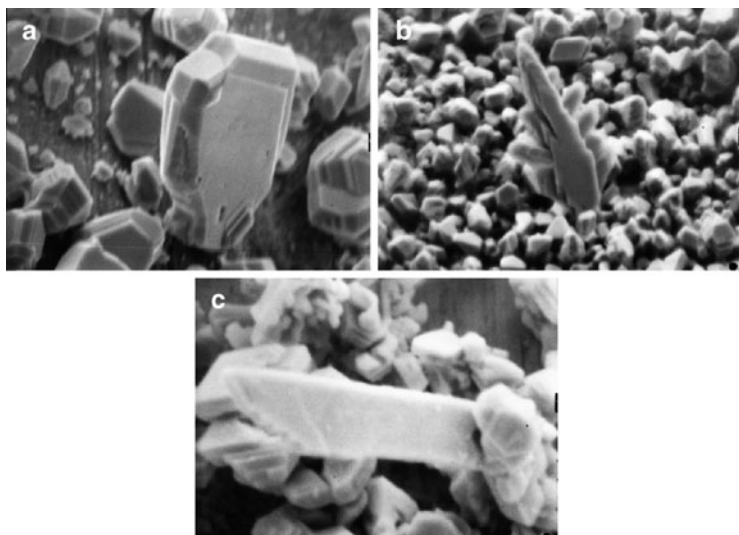
Fig. 2.22 Precursors of cadmium dendrites obtained by electrochemical depositions at overpotentials, η, of: (**a**) $\eta = 50$ mV; deposition time, $t = 2$ min; magnification: $\times 5000$; (**b**) $\eta = 110$ mV; $t = 2$ min; $\times 3000$; and (**c**) $\eta = 130$ mV; $t = 3$ min; $\times 9000$ (Reprinted from [53] and [54] with permission from Elsevier and [6] and [47] with permission from Springer.)

Precursors of cadmium dendrites [47] obtained by the processes of electrochemical deposition from 0.1 M $CdSO_4$ in 0.50 M H_2SO_4 onto cadmium wire electrodes at different overpotentials are shown in Fig. 2.22. It is obvious that further growth of the dendrite precursors shown in Fig. 2.22 leads to the formation of 2D dendrites (Fig. 2.23). Around the tips of dendrite precursors, as well as around the tips of dendrites, spherical or cylindrical diffusion control can occur, which is in good agreement with the requirements of the mathematical model.

There is an induction period before initiation of dendritic growth [25, 33, 49, 50]. During this induction period, dendrite precursors are formed by the growth of suitable nuclei. According to Pangarov and Vitkova [51, 52] the orientation of nuclei is related to the overpotential used. The effect of overpotential of electrodeposition on the shape of cadmium dendrites is illustrated in Fig. 2.23.
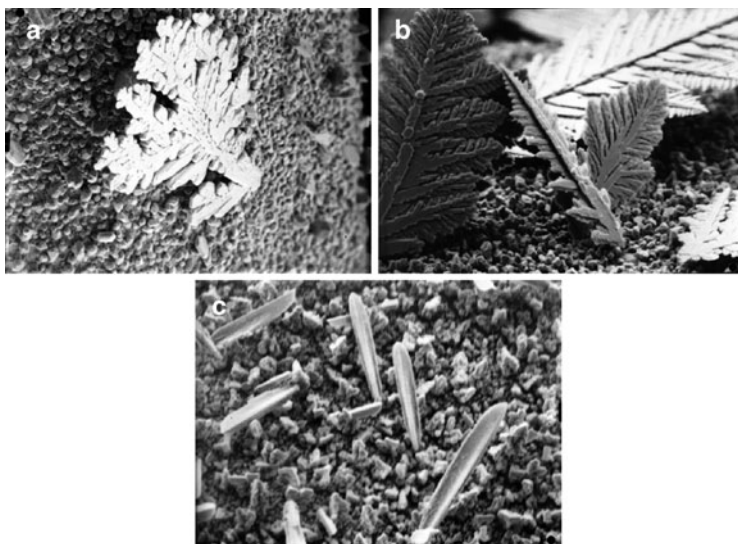
Fig. 2.23 Cadmium dendrites obtained at overpotentials, η, of: (**a**) $\eta = 50$ mV; $t = 10$ min; $\times 200$; (**b**) $\eta = 110$ mV; $t = 2$ min; $\times 400$; and (**c**) $\eta = 130$ mV; $t = 3$ min; $\times 1000$ (Reprinted from [53] with permission from Elsevier and [6] and [47] with permission from Springer.)

Most of the data concerning Co, Fe and Ni powders electrodeposition are summarized in Chapter XVIII of the book "Electrodeposition of Powders from Solutions," by Calusaru [55].

2.5 The Iron-Group Metal Powders

According to Calusaru [55] some information on electrodeposition of Co powder is available in patents [56] as well as in reviews [57]. Unfortunately these references are from 1932 and there are no data about the morphology of powder particles, since then there are no published data about electrodeposition of Co powder. Only two micrographs of Co powder, showing that the particles are very fine agglomerates, are presented in the Metallographic Atlas of Powder

Metallurgy [58], but the procedure of their production is not mentioned and it is stated that their typical application is for hard metal production.

Contrary to the limited data for Co and Ni powders electrodeposition, the highest number of 71 references for Fe powder electrodeposition exist in the book of Calusaru [55]. In this introduction only the most important ones are cited.

Because of its application in the manufacturing of porous metalloceramic bearings, of friction materials, parts for machinery, various alloys, in chemical industry, in manufacture of rechargeable batteries, etc., Fe powder is an important industrial product [55]. Significant amount of Fe powder is produced by electrochemical technique and 20% of electrodeposited Fe powders have to be blended with Fe powders produced by other procedures. The main advantage of electrodeposited Fe powder is its volumetric mass ($1.5–2.2$ g cm^{-2}) and its suitability for pressing, due to dendritic particle shape.

Generally speaking, in most of the electrolytes for Fe powder electrodeposition fragile deposits were obtained and transformed into powders by removal from the cathode surface and subsequent grinding [59–70]. Very few high purity Fe powders were obtained by electrodeposition. Usually these powders contain certain amount of oxides, mainly due to powder oxidation during the washing and drying procedure.

Three types of electrolytes were used for Fe powder electrodeposition (1) electrolytes based on sulfate salts [59–63]; (2) electrolytes based on chloride salts [65–69]; and (3) alkaline electrolytes: reduction of $Fe(OH)_2$ suspension in alkaline media [71]; formation of $Fe(OH)_3$, and its reduction from the suspension of Fe_3O_4 in alkaline solution [70].

Because of the possibility for $Fe(OH)_2$ or $Fe(OH)_3$ formation the suggested pH values for the electrolytes are pH < 3.

An interesting method for producing very fine Fe powder by the electrolysis in a two-layer electrolytic bath using a hydrocarbon solvent from an oil refining fraction as an upper organic layer has also been suggested [72]. It was also shown that in the presence of chelating agents, fine, nondendritic Fe powders could be obtained [73].

Two types of electrolytes for Ni powder electrodeposition were investigated: acid electrolytes [74–82] and ammoniacal electrolytes [74, 77, 83]. For acid electrolytes it is characteristic that the increase of current density and decrease of nickel ion concentration in solution cause a lowering of powder fragility. The powder is free from oxides and basic salts and dry powder could be stored in a dry place indefinitely without oxidation or structure change [74–82]. Characteristic of ammoniacal electrolytes is that the increase of ammonia concentration cause disperse and pure (without hydroxide impurities) deposit formation consisting of dark nickel particles of 4–10 μm and of larger particles of about 400 μm [74, 77, 83].

The influence of pulsating and reversing current regime on the Ni powder electrodeposition was investigated in the paper of Pavlović et al. [84]. It is found that the increase of frequency of pulsating current induces a decrease in particle size, while in the case of reversing current regimes the size of powder particles increase with increasing average current density.

2.5.1   Characterization of the Polarization Curves for Co, Fe, Ni Powders Electrodeposition

It is well known that the electrodeposition of the iron group metals (Co, Fe, Ni) occurs with simultaneous hydrogen evolution [85–89]. In such a case it is practically impossible to determine the diffusion limiting current density for their electrodeposition from the polarization curves (contrary to the case of the electrodeposition of Ag, Cu, Pd, etc) and define the beginning of powder formation expressed with the increase of current density over the diffusion limiting current density, corresponding to the process of simultaneous hydrogen evolution. To obtain correct polarization curves for the electrodeposition of these systems it is necessary to apply IR drop compensation technique. In all our cases the current interrupt technique was used, while polarization curves were recorded onto glassy carbon electrode.
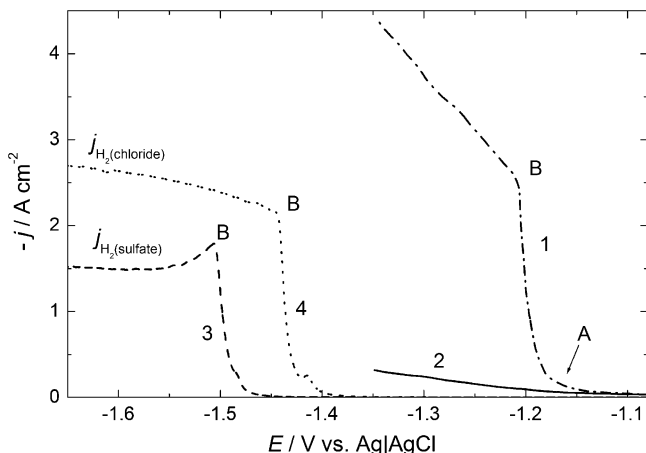
Fig. 2.24 Typical polarization curves for the electrodeposition of Co powder from ammonium sulfate–ammonium hydroxide supporting electrolyte with (1) and without (2) IR drop correction. Polarization curves for hydrogen evolution in different supporting electrolytes are also presented in the figure (*curves* 3 and 4) (Reprinted from [90, 91] with the permission of Elsevier.)

Polarization curves were recorded in a three-compartment standard electrochemical cell at the room temperature. The sweep rate was 1 mV s^{-1} and current interrupt was applied at each 0.5 s. The platinum foil counter electrode and the reference—saturated silver/silver chloride, Ag|AgCl—electrode were placed in separate compartments. The working electrode was glassy carbon disc ($d = 0.3$ cm) placed parallel to the counter electrode.

Typical polarization curves with (1) and without IR drop correction (2) are presented in Fig. 2.24. While recording polarization curves with and without IR drop correction for all investigated alloy powders electrodeposition, almost identical difference between curves with (1) and without IR drop correction (2) for all supporting electrolytes, as well as for all investigated systems is obtained. In Fig. 2.24 is shown an example for Co electrodeposition from ammonium sulfate containing supporting electrolyte [90, 91].

As can be seen after IR drop correction (dash-dot line—1) significantly different current response is obtained than the one measured

without IR drop correction (solid line—2), being characterized by a sudden increase of current density at the commencement of the electrodeposition process. As far as the electrodeposition started, hydrogen evolution also started and the processes of all metal electrodeposition were accompanied by hydrogen evolution in the whole range of investigated potentials. As a consequence, extremely high current densities were recorded (since at the pH 9.2–9.5 hydrogen is evolving from water molecules) and accordingly correction for IR drop caused significant change in the shape of the polarization curves. At the same time it is important to note that because of intensive hydrogen evolution already at the commencement of the process of the electrodeposition, Co powder formation took place at current densities as low as 0.3 A cm^{-2} (low in comparison with the maximum current density of 3–6 A cm^{-2}). The characteristic for all curves is that after sudden increase of current (in this case at about -1.17 V—point A) additional inflection point appeared on the polarization curves (B) at the potential of about -1.21 V with further change of current density showing linear increase with the potential.

2.5.1.1 Polarization Curves for Hydrogen Evolution onto Glassy Carbon Electrode

As shown in Fig. 2.24 in a pure supporting electrolytes (1 M $(NH_4)_2SO_4$ + 0.7 NH_4OH or 1 M NH_4Cl + 0.7 NH_4OH) polarization curves for hydrogen evolution, corrected for IR drop, are different than those for metal or alloy electrodeposition, and their shapes and positions on the potential scale depend on the anions present in a supporting electrolyte. In both electrolytes the increase of current density corresponding to the hydrogen evolution onto glassy carbon electrode (3 and 4) is seen to take place at more negative potentials than in the case of metal or alloy electrodeposition. It is interesting to note that the overpotential for hydrogen evolution in sulfate containing supporting electrolyte is for about 0.1 V higher than that in chloride containing supporting electrolyte. Such a behavior is a clear indication that the processes of Co electrodeposition catalyze the reaction of hydrogen evolution in both supporting electrolytes.

Concerning the shape of both polarization curves for hydrogen evolution it appears that such shape is a consequence of the so called electrode effect [92–97]. This phenomenon is connected with the hydrogen bubble formation at high current densities, so that at the inflection point B the formation of bubbles becomes the rate limiting step of the electrochemical process [96, 97]. Accordingly, the shape of the polarization curves for iron group metal and their alloy electrodeposition is also defined by the process of bubble formation since the current density for hydrogen evolution in all cases amounts to 70–85% of total current density.

2.5.1.2   Current Efficiency Determination

Taking into account that simultaneous hydrogen evolution occurs in all cases, it was necessary to determine the current density for hydrogen evolution (j_H), subtract it from the measured (corrected for IR drop) current density values (j_{tot}) given in Fig. 2.25a to obtain current densities for powders electrodeposition (in this case Co powder, j_{Co}). Hence, several values of current density on the polarization curve for Co powder electrodeposition were chosen and the volume of evolved hydrogen was determined in the burette. The current for hydrogen evolution ($\circ$) was obtained using the equation [98]

$$I_{H_2} = \frac{nFV}{tV_n} = \frac{nF}{V_n} \times \frac{V}{tT} = 2.3522 \times 10^3 \times \frac{V}{tT}, \tag{2.25}$$

where V—experimentally determined volume of the evolved hydrogen at P_{at} and $T = 298$ K corrected to the normal conditions ($P^{\ominus}$ and $T = 273$ K); t—time of hydrogen evolution under constant current; V_n—volume of 1 mol of hydrogen at normal conditions (22.4 dm^3 mol^{-1}); n—number of exchanged electrons, and F—Faraday's constant. Using this procedure polarization curve corresponding to Co powders electrodeposition ($\triangle$) was obtained.

The current efficiency ($\circ$) for the electrodeposition process was obtained from the relation
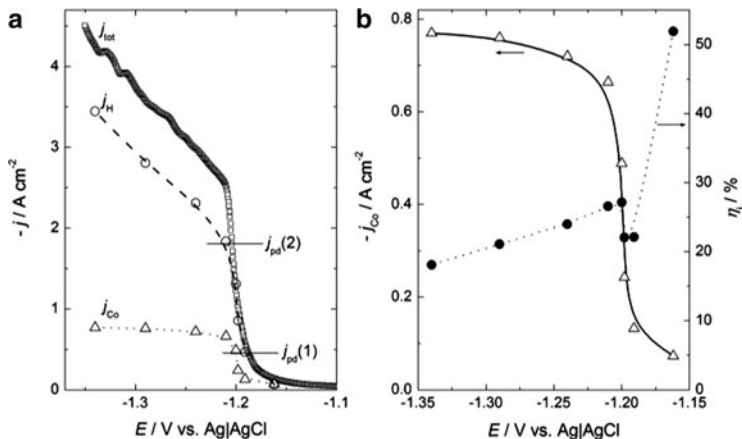
Fig. 2.25 (**a**) Polarization curve for the electrodeposition of Co powder after IR drop correction (j_{tot}), polarization curve for hydrogen evolution (j_H), and polarization curve for Co powder electrodeposition (j_{Co}) after subtraction of the current density for hydrogen evolution. (**b**) Polarization curve for Co powder electrodeposition (j_{Co}) and corresponding current efficiency curve (η_j) (Reprinted from [90, 91] with the permission of Elsevier.)

$$\eta_j(\%) = \frac{j_{Co}}{j_{tot}} \times 100 = \frac{j_{tot} - j_H}{j_{tot}} \times 100. \quad (2.26)$$

Corresponding values are presented in Fig. 2.25b.

As can be seen already at the beginning of the deposition process significant amount of hydrogen is evolving, causing the value of the current efficiency of about 52%. At more negative potentials this value decreases to about 20–25%, with the sharp decrease taking place in the region of the sharp increase in current density.

All powder samples for XRD analysis and morphology investigations were electrodeposited at the room temperature in the cylindrical glass cell of the total volume of 1 dm^3 with cone-shaped bottom of the cell to collect powder particles in it. Working electrode was a glassy carbon rod of the diameter of 5 mm, with the total surface area of 7.5 cm^2 immersed in the solution and placed in the middle of the cell. Cylindrical Pt–Ti mesh placed close to the cell

walls was used as a counter electrode providing excellent current distribution in the cell.

In all cases certain, small amount of disperse deposit remained on the glassy carbon electrode, while only powder particles that were detached from the electrode surface and collected at the cone-shaped bottom of the cell were analyzed.

2.5.2 Electrodeposition of Co Powder

Cobalt powder was electrodeposited from the solutions containing either sulfate or chloride anions.

2.5.2.1 Electrodeposition of Co Powder from Sulfate Electrolyte

The composition of the electrolyte was 1M $(NH_4)_2SO_4$ + 0.7 M NH_4OH + 0.1 M $CoSO_4$, pH 9.5. Polarization curves were recorded on the glassy carbon disc by the procedure explained in Sect. 2.5.1. The powders for SEM and XRD analyses were electrodeposited at two constant current densities (see Fig. 2.25a): $j_{pd}(1) = -0.50$ A cm^{-2} and $j_{pd}(2) = -1.85$ A cm^{-2}.

The polarization curve and the corresponding current efficiency potential dependence are presented in Fig. 2.25b. The process of Co electrodeposition commences at about -1.10 V with the second inflection point being placed at -1.20 V. The curve for Co powder electrodeposition (j_{Co}) is characterized with well-defined current density plateau in the potential range between -1.20 V and -1.35 V, indicating that at potentials more negative than -1.20 V diffusion limiting current density for Co powder electrodeposition is reached in Fig. 2.25a. The current efficiency (η_j), obtained using equation (2.26), is seen to decrease sharply from about 52% to about 20% in the potential range of sharp increase of current density on the polarization curve j_{Co} vs. E in Fig. 2.25b. At potentials more negative than -1.20 V, η_j vs. E dependence slightly decreases from about 27% to about 20%.
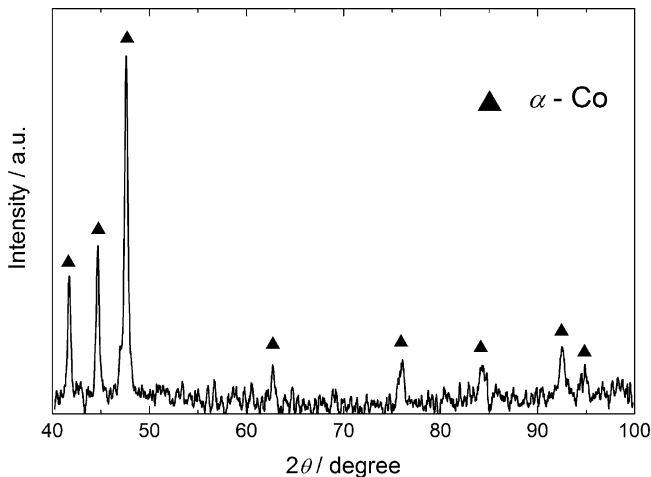
Fig. 2.26 X-ray diffraction pattern of electrodeposited cobalt powders (Reprinted from [99] with the permission of Springer-Verlag.)

X-ray diffraction pattern for Co powder samples electrodeposited either with $j_{pd}(1)$ or $j_{pd}(2)$, from sulfate or chloride electrolytes, is shown in Fig. 2.26. As can be seen the powder consists only of the hexagonal close-packed α-cobalt phase with the lattice parameters of $a = 2.5007$ Å and $c = 4.0563$ Å. No hydroxide or oxide impurities were detected [99].

In the case of Co powder electrodeposition at lower current density ($j_{pd}(1) = -0.50$ A cm^{-2}), generally two types of agglomerates are detected [99]:

1. Dendrite particles varying in the size from about 5 μm to about 50 μm, as shown in Fig. 2.27a.
2. Different types of agglomerates varying in the size from about 100 μm to about 500 μm, as it is shown in Fig. 2.27b–d. These agglomerates can further be divided into three groups:

   (a) Compact agglomerates of the size of about 200 μm to about 500 μm, composed of smaller agglomerates of the size of about 20 μm to about 50 μm, Fig. 2.27b. These agglomerates are characterized with the presence of deep cylindrical
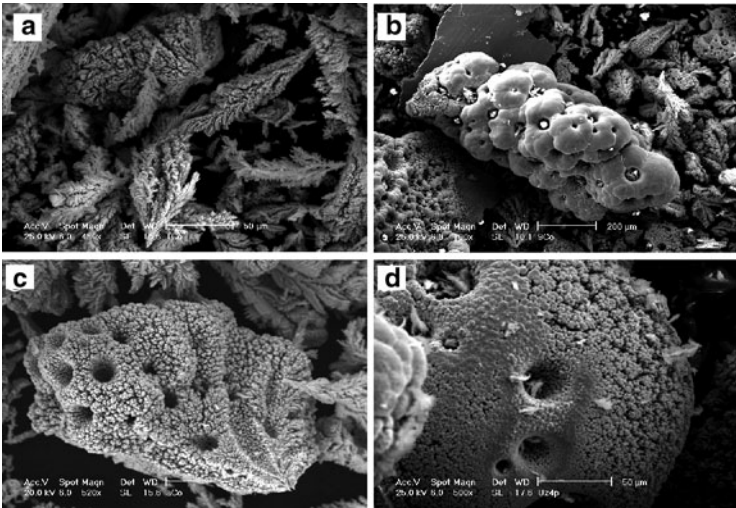
Fig. 2.27 Typical particles detected in the electrodeposited cobalt powder (Reprinted from [99] with the permission of Springer-Verlag.)

cavities and fern-like dendrites formed on the bottom of most of the cavities.

(b) Spongy-like agglomerates of different shapes varying in size from about 100 μm to about 200 μm with the fern-like dendrites also formed on the bottom of most of the cavities, Fig. 2.27c.

(c) Balls of the size of about 200 μm containing deep cavities with the fern-like dendrites formed on the bottom of most of the cavities and more or less dense cauliflower structure on the surface of these balls, as shown in Fig. 2.27d.

In Figs. 2.28a–d and 2.29a, b cross sections of some of the agglomerates detected in the Co powder deposit are shown.

As can be seen they are in good agreement with the SEM results: Fig. 2.28b ball-like particles; Fig. 2.28c spongy particles; Fig. 2.28d compact agglomerates. Although for Co powder different types of agglomerates are present, it is quite obvious that all Co powder
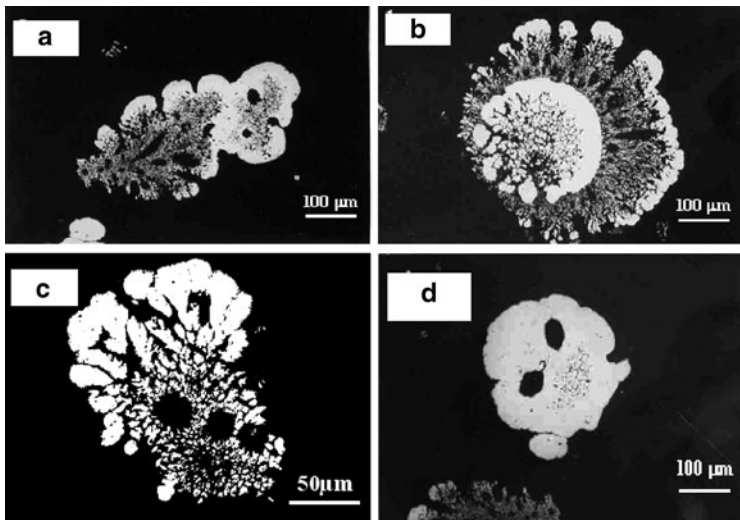
Fig. 2.28 Cross sections of some of the agglomerates detected in the Co powder deposit (Reprinted from [99] with the permission of Springer-Verlag.)
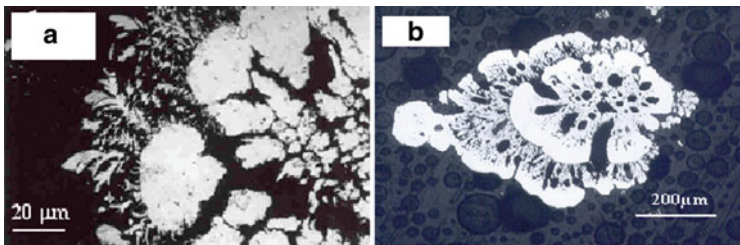

Fig. 2.29 Cross sections of some of the agglomerates detected in the Co powder deposit (Reprinted from [99] with the permission of Springer-Verlag.)

agglomerates are characterized with the presence of large number of cavities. A common characteristic of these cavities for all types of agglomerates (Fig. 2.27) is the presence of small fern-like dendrites on the bottom of most of the cavities.

2.5.2.2 Mechanism of Co Powder Electrodeposition

Considering cross sections of some of the agglomerates detected in the Co powder deposit [99], Figs. 2.28 and 2.29, it appears that they are all different, not only because different types of agglomerates have been detected but also because some pictures represent cross sections of the agglomerate parallel to the line of its growth (Fig. 2.28a), while some pictures represent cross sections of the agglomerate normal to the line of its growth (Fig. 2.28b–d). It has already been explained in the literature [100] that in the case of dendrite particles, depending on their length, it is possible that the morphology of the dendrite changes from disperse one to a compact one, as shown in Fig. 2.28a. This agglomerate seems to grow from the left to the right side.

With the time of growth the disperse agglomerate is branching in different directions and at the tip of each branch spherical diffusion is taking over the planar one, providing conditions for the growth of compact deposit as a consequence of the decrease of the local current density on the tip of each branch. After some time, these branches form compact deposit all over the agglomerate surface and the same agglomerate further grows as a compact one (right side of the particle), until it falls off from the electrode surface. In Fig. 2.28b it is most likely that a compact part of the agglomerate represents the picture of the cross section normal to the line of its growth. Depending on the way of growth, the moment of detaching agglomerate from the electrode surface and the position at the electrode surface where some agglomerate started to grow, different shapes of agglomerates are obtained (Fig. 2.28a–d), but all of them show the same characteristic of transforming disperse into compact deposit with increase in their size.

A special case is the formation of the balls of the size from about 200 μm containing deep cavities with the fern-like dendrites formed on the bottom of cavities and more or less dense cauliflower structure on the surface of these balls, Fig. 2.27d. The cross section of such agglomerate is shown in Fig. 2.28b. For some reasons this agglomerate started to grow as a ball, again starting from disperse (in the middle) and finishing with compact deposit at the surface for a reason

already explained. After some time of the growth of compact deposit the conditions for planar diffusion were restored causing the formation of dendrites all over the ball surface. It should be noted that at the same time there was a local increase of overpotential due to reduction of the active surface area as a result of compact deposit formation. Dendrites were growing normal to the ball surface, and again after some time spherical diffusion took over the control of the planar one and dendrites started transforming into compact deposit. Since dendrites were not dense, they were not able to form compact deposit all over the agglomerate surface when the agglomerates detached from the electrode surface.

A cross section of one of the agglomerates parallel to the line of its growth is shown in Fig. 2.29b. As can be seen, in accordance with the previous statement, after the first front of compact deposit has been formed, disperse deposit started to grow and for the same reasons its growth finished as a compact deposit at the moment when this agglomerate detached from the electrode surface.

It is necessary to note that almost all morphological forms presented in this chapter can be explained by the above discussion, being dependent on the stage of the agglomerates, i.e., the moment when they detached from the electrode surface. It is most likely that the form presented in Fig. 2.30 should be considered as the initial stage of the growth of a second generation of dendrites, clearly detected on a cross section of ball-like particles presented in Fig. 2.29a.

Quite unique feature of all agglomerates detected in Co powder deposit is the presence of deep cavities on their surfaces and the fern-like dendrites on their bottom for most of the cavities. This is illustrated in Fig. 2.27b for compact agglomerates and in Fig. 2.27d for ball-like agglomerates. The most interesting one is the cavity detected in the ball-like agglomerates. More detailed micrograph for such cavity is shown in Fig. 2.31.

It is most likely that these cavities are the consequence of hydrogen bubble formation, preventing deposition inside the cavity. Once the bubble is liberated, the conditions for the growth of fern-like dendrites are fulfilled at the bottom of the cavity due to current distribution and restored planar diffusion. Since this agglomerate is not dense, crystals of different size can be seen in the cavity, with less
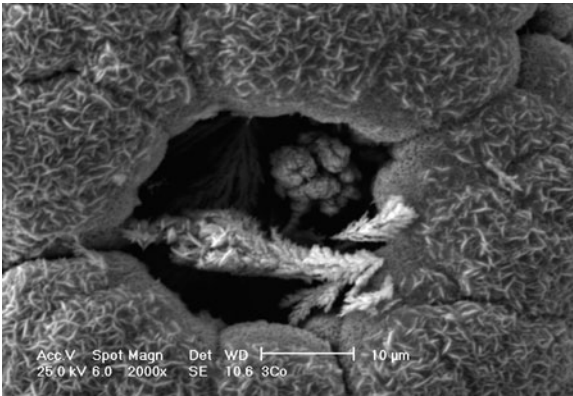
Fig. 2.30 SEM micrograph of the surface of compact agglomerate with the initial stage of the growth of a second generation of dendrites (Reprinted from [99] with the permission of Springer-Verlag.)
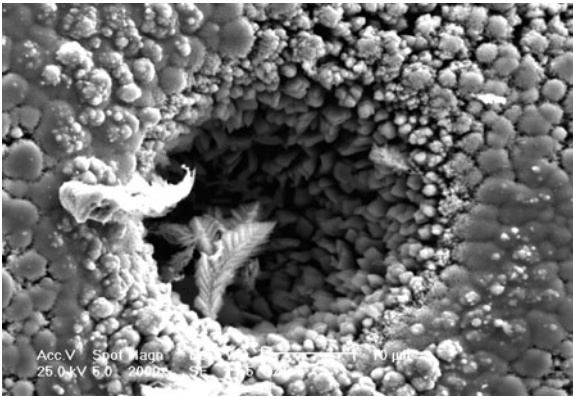

Fig. 2.31 SEM micrograph of the cavity detected on the ball-like agglomerate (Reprinted from [99] with the permission of Springer-Verlag.)

dense ones placed at the bottom and more dense ones placed close to the top of the cavity. We believe that such distribution of crystals is the consequence of current distribution over the hydrogen bubble, while at the moment of bubble liberation fern-like dendrite starts

growing at the bottom of cavity in the same way as the dendrite precursors in the diffusion layer of the macroelectrode [101]. At that moment spherical diffusion is restored at the edges of cavity and compact deposit is obtained all around the cavity.

Concerning spongy deposits, it should be emphasized here that in comparison with other morphologies, traditionally called spongy, presented in the literature [47, 102] so far, the morphology of particles shown in Fig. 2.27c represents the real spongy deposit and that such similarity with the sponge has never been presented so far.

The morphology of Co powder electrodeposited at higher current density ($j_{pd}(2) = -1.85$ A cm^{-2}) is much more uniform in comparison with the morphology of Co powder electrodeposited at a lower current density.

Independently of the substrate (Co powders were electrodeposited onto GC, Co, and Ni electrodes) all agglomerates possessed spongy-like shapes, some of them being bigger (about 600 μm, Fig. 2.32a), while most of the agglomerates were of the order of 100–200 μm, Fig. 2.32b, c. The best sample for the formation of such agglomerates is presented in Fig. 2.32c. They start growing as dendrites (marked with arrow ←1) and after some time, for the reasons explained earlier, their surfaces become compact and characterized with the presence of two types of cavities (as a consequence of hydrogen bubbles formation on the agglomerate surfaces): cone-shaped ones (marked with arrow 2→) and cylindrical ones (marked with arrow ←3, identical to those obtained for Co powders electrodeposited at lower current density, $j_{pd}(1) = -0.50$ A cm^{-2}). It is interesting to note that fern-like dendrites were not formed on the bottom of cylindrical cavities, indicating that the agglomerates were detached from the electrode surface before the liberation of hydrogen bubbles formed on their surfaces. Hence, the electrolyte did not enter the cavities providing conditions for planar diffusion inside the cavity and the growth of fern-like dendrites. This is reasonable to expect since the time for agglomerates detaching should be much shorter for more intensive hydrogen evolution at $j_{pd}(2)$.

Considering Fig. 2.32 it can be concluded that most of the agglomerate surfaces are covered with very flat nodular endings. By the investigation of these surfaces at higher magnification it is discovered
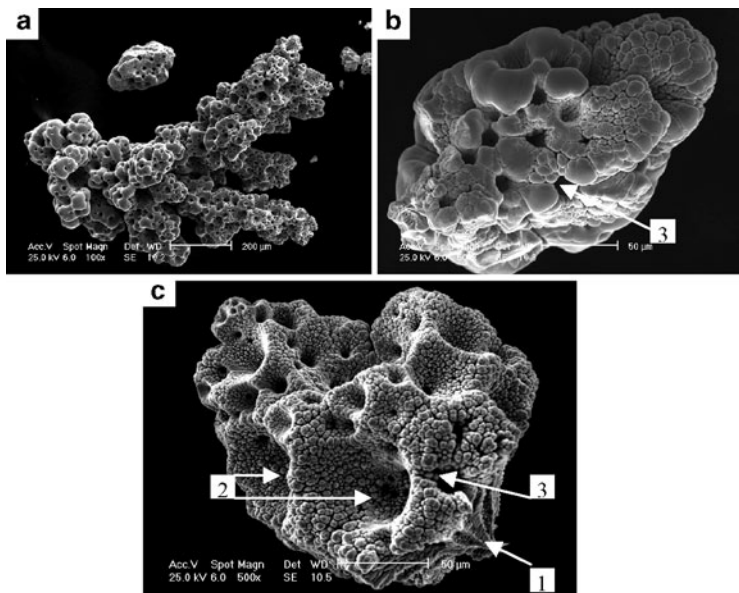
Fig. 2.32 SEM micrographs of the agglomerates electrodeposited at high current density

that these flat surfaces are actually composed of very thin (about 0.1 μm) and about 1 μm long crystals of Co, as shown in Fig. 2.33.

2.5.2.3 Electrodeposition of Co Powder from Chloride Electrolyte

The composition of the electrolyte was 1M NH_4Cl + 0.7 M NH_4OH + 0.1 M $CoCl_2$, pH 9.4. Polarization curves were recorded on the glassy carbon (GC) and Co discs. The powders for SEM and XRD analyses were electrodeposited at a constant current density of -2.00 A cm^{-2} onto GC electrode and -0.77 A cm^{-2} onto Co electrode.

The polarization curve and the corresponding current efficiency potential dependence recorded onto GC electrode are presented in Fig. 2.34. The shape of the polarization curve in Fig. 2.34a is
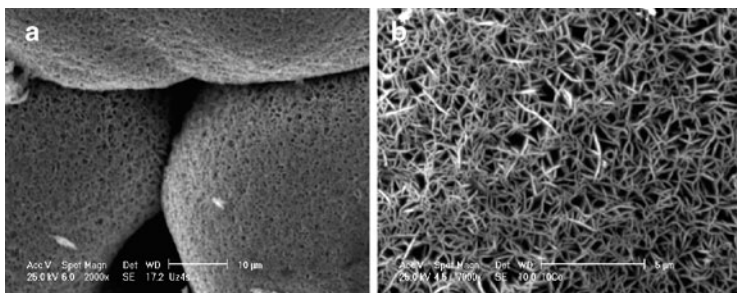
Fig. 2.33 Structure of the flat nodular endings detected on the surfaces of agglomerates electrodeposited at high current density. The same structure was detected on compact agglomerates electrodeposited at low current density
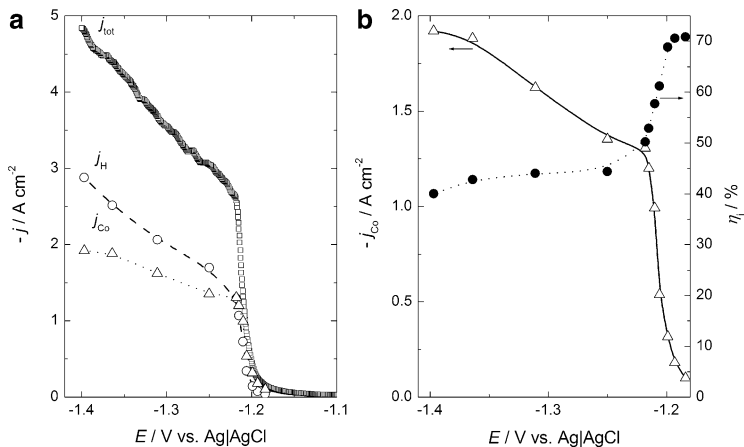

Fig. 2.34 (**a**) Polarization curve for the electrodeposition of Co powder after IR drop correction (j_{tot}), polarization curve for hydrogen evolution (j_H) and polarization curve for Co powder electrodeposition (j_{Co}) after subtraction of the current density for hydrogen evolution. (**b**) Polarization curve for Co powder electrodeposition (j_{Co}) and corresponding current efficiency curve (η_j) (Reprinted from [90, 91] with the permission of Elsevier.)

identical to the one recorded for Co powders electrodeposition from sulfate electrolyte (Fig. 2.25a). As can be seen in Fig. 2.34 the process of Co electrodeposition commences at about −1.10 V with the second inflection point being placed at −1.21 V. The curve for Co
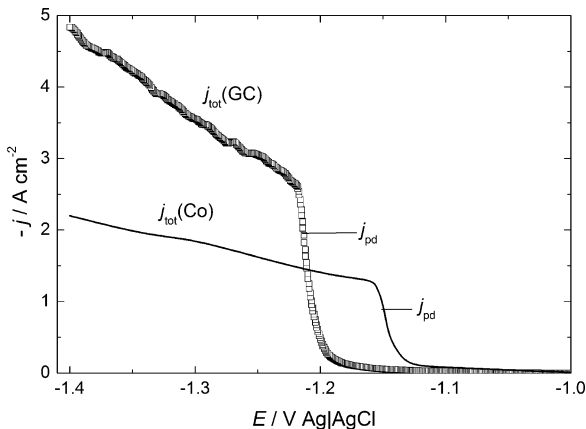
Fig. 2.35 Polarization curves for the electrodeposition of Co powder after IR drop correction (j_{tot}) recorded onto GC electrode ($j_{tot}(GC)$) and onto Co electrode ($j_{tot}(Co)$)

powder electrodeposition (j_{Co}) in this case is not characterized with well-defined current density plateau in the potential range between −1.21 V and −1.40 V as was in the case sulfate electrolyte, Fig. 2.25a. A linear increase of the current density for Co powder electrodeposition (j_{Co}) is most likely due to the increase of real surface area of the electrode covered with compact deposit and/or different intensity of hydrogen evolution in this electrolyte. The current efficiency (η_j) is seen to decrease sharply from about 70% to about 45% in the potential range of sharp increase of current density on the polarization curve j_{Co} vs. E in Fig. 2.25b. At potentials more negative than −1.20 V, η_j is practically independent of potential value.

Comparing polarization curves (j_{tot}) recorded onto GC and Co electrodes (Fig. 2.35) one can see that the electrodeposition process onto Co electrode commences at more positive potentials, while the current density of the second inflection point, as well as the current density at potentials more negative than that point, is smaller. Such behavior is reasonable to expect since the overvoltage for Co electrodeposition should be higher for GC than for Co electrodes, while at the same time the increase of the real surface area onto Co
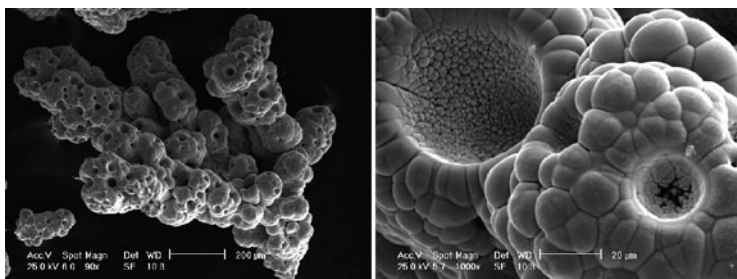
Fig. 2.36 SEM micrographs of the agglomerates electrodeposited at j_{pd} marked in Fig. 2.11 for GC and Co electrode (Reprinted from [91] with the permission of Elsevier.)

electrode should be smaller than that on the GC electrode since the epitaxial growth of Co onto Co electrode should be expected at the beginning of the electrodeposition process.

The morphology of Co powder agglomerates electrodeposited at j_{pd} (marked in Fig. 2.35), independently of the substrate (GC or Co), is presented in Fig. 2.36. It is practically the same as that for Co powder electrodeposited at $j_{pd}(2)$ from sulfate electrolyte [90], except that all nodular endings possess flat surface [91] which is actually composed of very thin (about 0.1 μm) and about 1 μm long crystals of Co, as shown in Fig. 2.33.

2.5.3 Electrodeposition of Fe Powder

Iron powder was electrodeposited from the solution containing 1 M NH_4Cl + 0.2 M $Na_3C_6H_5O_7$ + 0.1 M $FeCl_2$, pH 4.0. Polarization curves were recorded on the glassy carbon disc by the procedure explained in Sect. 2.5.1. The powders for SEM and XRD analyses were electrodeposited at the current density j_{pd} (marked in Fig. 2.37) by the procedure explained in Sect. 2.5.1.

The polarization curve for Fe powder electrodeposition is shown in Fig. 2.37. The current efficiency for Fe powder electrodeposition is very small ($<2\%$) and the polarization curves for Fe powder
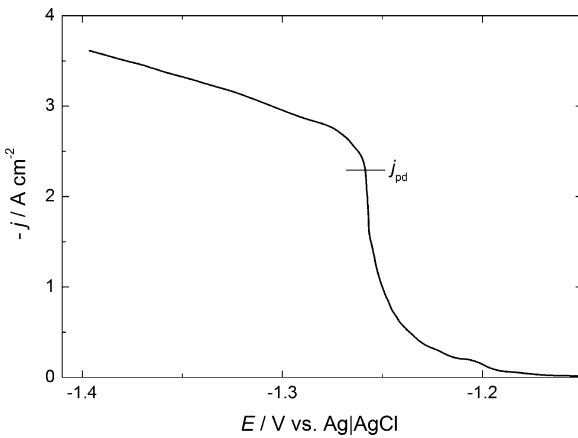
Fig. 2.37 Polarization curve for Fe powder electrodeposition

electrodeposition (j_{tot}) and for hydrogen evolution (j_H) practically overlap. Accordingly, η_j vs. E is not presented [103].

The diffractogram of electrodeposited Fe powder is presented in Fig. 2.38. The dimensions of crystallites were about 20 nm. Because of very small dimensions of crystallites only phases with the highest intensity were determined with high certainty, and these were peaks of the α—Fe phase (▲).

Agglomerates of the order of 100–200 μm with big cone-shaped cavities in Fig. 2.39a and small number of deep cylindrical cavities Fig. 2.39b are characteristic for this powder, as shown in Fig. 2.39 [103].

The surface of nodular endings on the agglomerates is not as flat as in the case of Co powder agglomerates, and the formation of new crystals on compact surface can be detected (Fig. 2.39b).

2.5.4 Electrodeposition of Ni Powder

Electrodeposition of Ni powder was investigated from three different solutions: 1 M $(NH_4)_2SO_4$ + 0.7 M NH_4OH + 0.1 M $NiSO_4$—sulfate solution; 1 M NH_4Cl + 0.7 M NH_4OH + 0.1 M $NiCl_2$—chloride
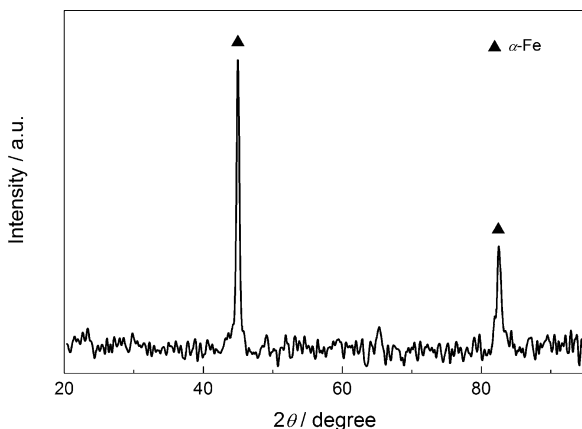
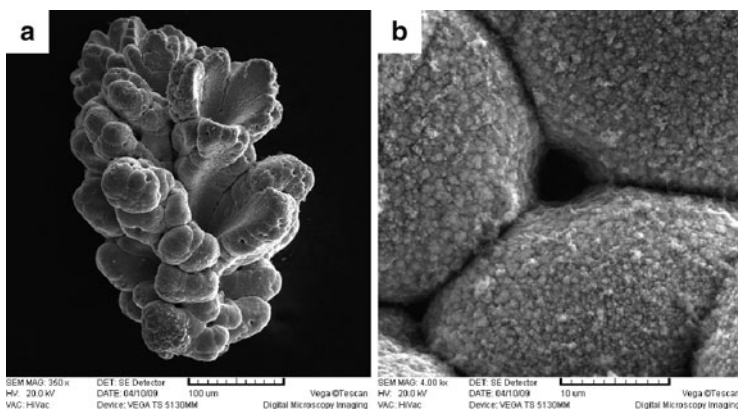**Fig. 2.38** X-ray diffraction pattern of electrodeposited Fe powder

Fig. 2.39 (**a**) SEM micrograph of the agglomerates obtained in electrodeposited Fe powder. (**b**) Deep cylindrical cavity surrounded with spherical compact surface covered with new crystals (Reprinted from [103] with the permission of Elsevier.)

solution; and 1M NH_4Cl + 0.2 M $Na_3C_6H_5O_7$ + 0.1 M $NiCl_2$—citrate solution.

The polarization curve and the corresponding current efficiency potential dependence recorded onto GC electrode from sulfate solution are shown in Fig. 2.40.
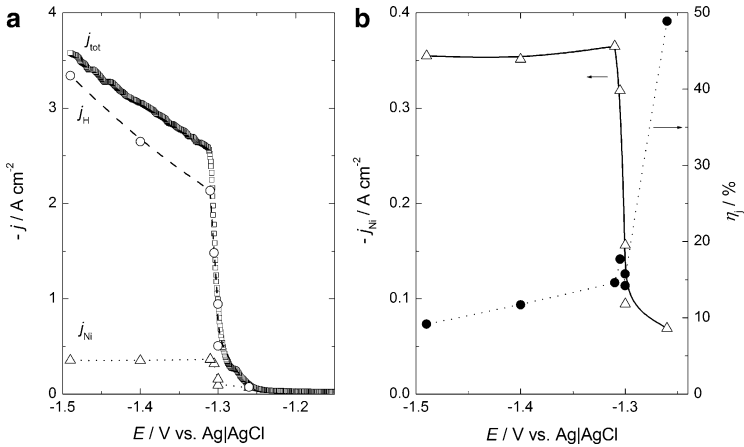
Fig. 2.40 (**a**) Polarization curve for the electrodeposition of Ni powder from sulfate solution after IR drop correction (j_{tot}), polarization curve for hydrogen evolution (j_H) and polarization curve for Ni powder electrodeposition (j_{Ni}) after subtraction of the current density for hydrogen evolution. (**b**) Polarization curve for Ni powder electrodeposition (j_{Ni}) and corresponding current efficiency curve (η_j) (Reprinted from [90] with the permission of Elsevier.)

The process of Ni electrodeposition commences at about −1.25 V with the second inflection point at −1.30 V. The curve for Ni powder electrodeposition (j_{Ni}) is characterized with well-defined current density plateau in the potential range between −1.30 V and −1.40 V. The current efficiency (η_j) is seen to decrease sharply from about 50% to about 15% in the potential range of sharp increase of current density on the polarization curve j_{Ni} vs. E in Fig. 2.40b. At potentials more negative than −1.30 V η_j slightly decreases to about 10% at −1.40 V.

The polarization curve and the corresponding current efficiency potential dependence recorded onto GC electrode from chloride solution [91] are shown in Fig. 2.41. As can be seen in Fig. 2.41a the electrodeposition of Ni in this solution commences at slightly more negative potential of about −1.28 V, while j_H is lower than that recorded in sulfate solution and accordingly the current efficiency (η_j) is higher, sharply decreasing from about 90% to about 45% in the potential range of sharp increase of current density on the
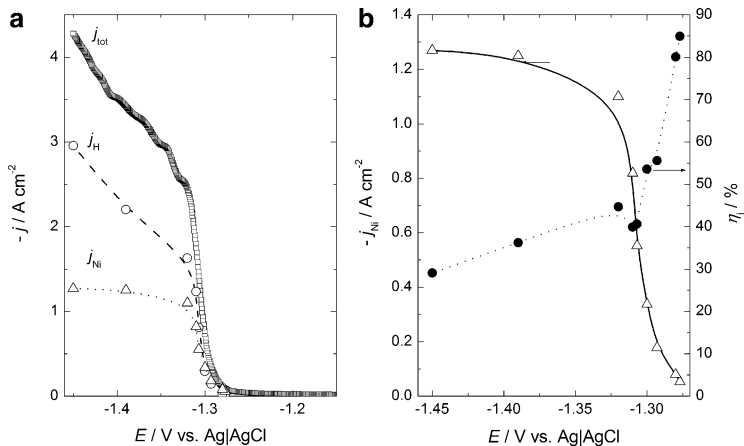
Fig. 2.41 (**a**) Polarization curve for the electrodeposition of Ni powder from chloride solution after IR drop correction (j_{tot}), polarization curve for hydrogen evolution (j_H), and polarization curve for Ni powder electrodeposition (j_{Ni}) after subtraction of the current density for hydrogen evolution. (**b**) Polarization curve for Ni powder electrodeposition (j_{Ni}) and corresponding current efficiency curve (η_j) (Reprinted from [91] with the permission of Elsevier.)

polarization curve j_{Ni} vs. E in Fig. 2.41b. At potentials more negative than -1.30 V η_j slightly decreases to about 30% at -1.40 V.

The polarization curve recorded onto GC electrode from citrate solution is compared with those from sulfate and chloride solutions in Fig. 2.42. Similar polarization curves from all solutions are obtained, except that the current density after the second inflection point for citrate solution is half of that for sulfate and chloride solutions. The (η_j) vs. E dependence recorded in citrate solution is similar to those for sulfate and chloride solutions, being practically constant (20%) in the potential range of current density plateau on the polarization curve j_{Ni} vs. E.

Samples for SEM, EDS, and XRD analyses were electrodeposited at the j_{pd} values marked in the figure, $j_{pd}(sul) = -0.5$ A cm^{-2}, $j_{pd}(chl) = -2.0$ A cm^{-2}, $j_{pd}(cit) = -1.4$ A cm^{-2}.

X-ray diffraction pattern of nickel powder sample is shown in Fig. 2.43. The same diffractograms are obtained for Ni powders electrodeposited from all three solutions. As can be seen the powder
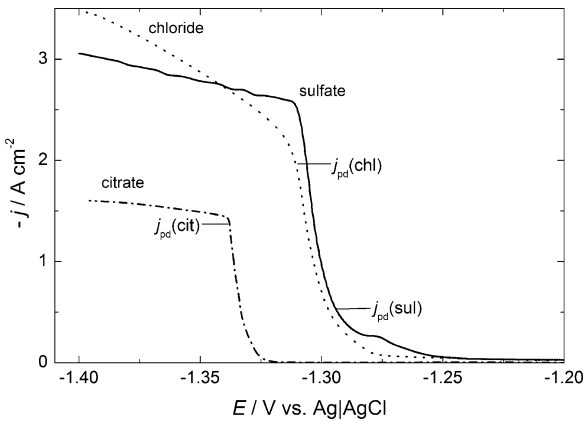
Fig. 2.42 Polarization curves for the electrodeposition of Ni powder from citrate, sulfate and chloride solutions after IR drop correction; corresponding current densities for powder electrodeposition, j_{pd}(cit), j_{pd}(sul), and j_{pd}(chl) are marked in the figure

consists only of the face-centered cubic nickel phase (β-Ni) with the lattice parameter of $a = 3.5231$ Å.

In Fig. 2.44a, b are shown SEM micrographs of Ni powder electrodeposited from sulfate solution at j_{pd}(sul) $= -0.5$ A cm^{-2}. As can be seen typical cauliflower-type agglomerates are obtained with the size of agglomerates varying from about 5 μm to about 50 μm. No hydroxide or oxide impurities were detected, which is in accordance with the literature data [74, 77, 83]. Ni powder agglomerates are very similar to those of copper [102] and since the mechanism of their growth has already been explained, it is not necessary to discuss the mechanism of their growth.

SEM micrographs of Ni powder electrodeposited from chloride solution at j_{pd}(chl) $= -2.0$ A cm^{-2} are shown in Fig. 2.45a, b. Typical spongy-like agglomerates are obtained with the size of agglomerates varying from about 200 μm to about 600 μm. As in the case of Co powder electrodeposited at high current densities from chloride and sulfate solution, cone-shaped (Fig. 2.45a) and cylindrical cavities (Fig. 2.45b) are obtained on the surface of Ni agglomerates. No fern-like dendrites were formed on the bottom of cylindrical cavities, indicating that the agglomerates were detached
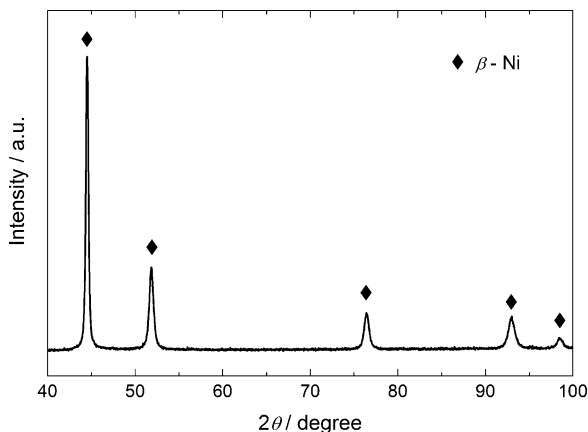
Fig. 2.43 X-ray diffraction pattern of electrodeposited Ni powder (Reprinted from [99] with the permission of Springer-Verlag.)
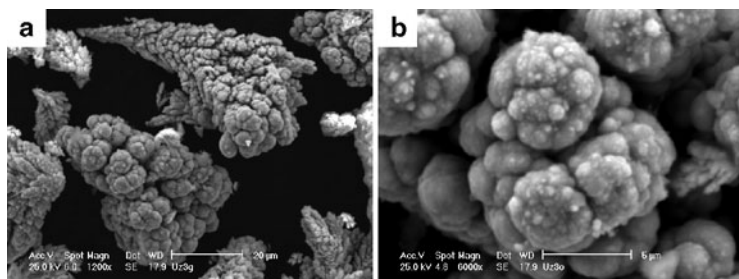

Fig. 2.44 SEM micrographs of the agglomerates electrodeposited at j_{pd}(sul) marked in Fig. 2.42 for GC electrode (Reprinted from [90] with the permission of Elsevier.)

from the electrode surface before the liberation of hydrogen bubbles formed on their surfaces, as explained in Sect. 2.5.2.2.

From the citrate solution completely different morphology of electrodeposited Ni powder is obtained [103], as shown in Fig. 2.46. Typical Ni powder is characterized by the presence of flake-like particles of the maximum size of about 50 μm covered with nodules of mainly flat surfaces. The formation of a second zone of
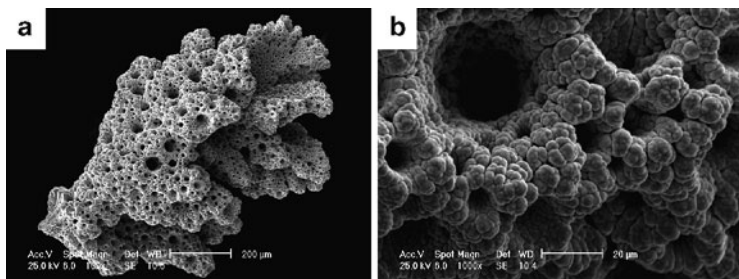
Fig. 2.45 SEM micrographs of the agglomerates electrodeposited at j_{pd}(chl) marked in Fig. 2.42 for GC electrode (Reprinted from [91] with the permission of Elsevier.)
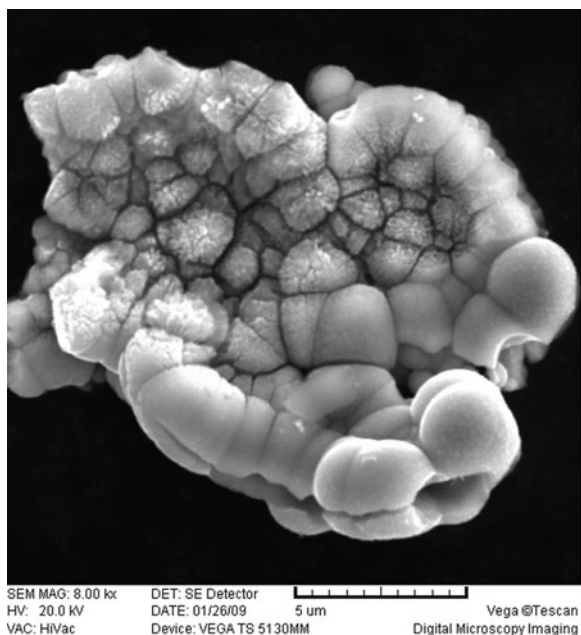

Fig. 2.46 Typical Ni powder particle electrodeposited at j_{pd}(cit) in citrate solution (Reprinted from [103] with the permission of Elsevier.)

dendrites (beginning with the formation of small crystals in the upper part of the particle presented in Fig. 2.46), typical for powder deposition [99], could be detected on some particles.

2.6   Conclusions

Powders of both academically and technologically important metals, such as silver, lead, cadmium, cobalt, nickel, and iron, were produced by the electrolytic processes. The constant regimes of electrolysis and the regime of pulsating overpotential (PO) were used for the electrochemical synthesis of powders of these metals. Morphologies of such obtained powders were characterized by the scanning electron microscopy and optical microscopy, as well as by X-ray diffraction techniques.

The processes of electrochemical deposition of silver from nitrate solutions, lead, and cadmium are characterized by high exchange current densities, and single and two-dimensional (2D) dendrites were largely formed by electrodepositions of these metals. On the other hand, very branchy dendrites constructed from corncob-like elements (similar to copper dendrites) were obtained by the electrodeposition of silver from ammonium solution which is characterized by the medium exchange current density. Also, the application of the PO regime strongly affected the morphology of silver and lead powder particles and mathematical model was presented to explain the change of morphology of particles in relation to the one obtained in the constant potentiostatic mode.

Ni powder is characterized by cauliflower-like type particles in ammoniacal electrolytes, while in citrate electrolytes the flakes of the maximum size of about 50 μm covered with nodules of mainly flat surfaces were detected. On some particles the formation of a second zone of dendrites (beginning with the formation of small crystals) could be detected. The Fe powder particles of the size of about 200 μm also contain nodules of flat surfaces, but they are characterized by the presence of cone-shaped cavities. In the case of Co powder, generally two types of particles were detected

(1) dendrite particles and (2) different types of agglomerates being characterized by the presence of cavities and fern-like dendrites formed on the bottom of most of them. These agglomerates can further be divided into three groups (a) compact agglomerates; (b) spongy-like agglomerates of different shapes, and (c) balls of the size of about 200 μm with more or less dense cauliflower structure on their surface. The growth mechanism of all agglomerates detected in the electrodeposited Co powder has been explained. The type of the agglomerate depends on its growth stage, i.e., on the moment when it becomes detached from the electrode surface.

References

1. Pavlović MG, Popov KI (2005) Electrochem Encycl. http://electrochem. cwru.edu/ed/encycl/
2. Winand R (1998) Electrochim Acta 43:2925
3. Price PB, Vermilyea DA (1958) J Chem Phys 28:720
4. Djokić SS, Nikolić ND, Živković PM, Popov KI, Djokić NS (2011) ECS Trans 33:7
5. Popov KI, Krstajić NV, Popov SR (1984) Surf Technol 22:245
6. Popov KI, Djokić SS, Grgur BN (2002) Fundamental aspects of electrometallurgy. Kluwer Academic/Plenum, New York
7. Nikolić ND, Popov KI, Pavlović LjJ, Pavlović MG (2006) J Electroanal Chem 588:88
8. Nikolić ND, Popov KI, Pavlović LjJ, Pavlović MG (2006) Surf Coat Technol 201:560
9. Nikolić ND, Popov KI, Pavlović LjJ, Pavlović MG (2007) Sensors 7:1
10. Nikolić ND, Branković G, Pavlović MG, Popov KI (2008) J Electroanal Chem 621:13

11. Nikolić ND, Popov KI (2010) Hydrogen co-deposition effects on the structure of electrodeposited copper. In: Djokić SS (ed) Electrodeposition: theory and practice, vol 48, Modern aspects of electrochemistry. Springer, New York, pp 1–70
12. Nikolić ND, Pavlović LjJ, Pavlović MG, Popov KI (2007) Electrochim Acta 52:8096
13. Nikolić ND, Pavlović LjJ, Branković G, Pavlović MG, Popov KI (2008) J Serb Chem Soc 73:753
14. Nikolić ND, Pavlović LjJ, Pavlović MG, Popov KI (2008) Powder Technol 185:195
15. Nikolić ND, Branković G, Pavlović MG, Popov KI (2009) Electrochem Commun 11:421
16. Nikolić ND, Branković G, Maksimović VM, Pavlović MG, Popov KI (2010) J Solid State Electrochem 14:331
17. Nikolić ND, Branković G, Maksimović VM, Pavlović MG, Popov KI (2009) J Electroanal Chem 635:111
18. Nikolić ND, Branković G, Popov KI (2011) Mater Chem Phys 125:587
19. Nikolić ND, Branković G (2010) Electrochem Commun 12:740
20. Nikolić ND, Branković G, Maksimović V (2012) J Solid State Electrochem 16:321
21. Popov KI, Vojnović M, Rikovski G (1968) Hemijska Industrija 8:1392 (in Serbian)
22. Trasatti S (1972) J Electroanal Chem 39:163
23. Popov KI, Pavlović MG, Stojilković ER, Radmilović V (1996) J Serb Chem Soc 61:47
24. Pavlović MG, Maksimović MD, Popov KI, Kršul MB (1978) J Appl Electrochem 8:61
25. Barton JL, Bockris JO'M (1962) Proc R Soc A268:485
26. Bek RYu, Kudryavtsev NT (1961) Zh Prikl Khim 34:2013
27. Bek RYu, Kudryavtsev NT (1961) Zh Prikl Khim 34:2020
28. Arouete S, Blurton KF, Oswin HG (1969) J Electrochem Soc 116:166
29. Popov KI, Keča DN, Anđelić MD (1978) J Appl Electrochem 8:19
30. Popov KI, Anđelić MD, Keča DN (1978) Glasnik Hem Društva Beograd 43:67
31. Popov KI, Pavlović MG, Remović GŽ (1991) J Appl Electrochem 21:743
32. Popov KI, Maksimović MD, Zečević SK, Stojić MR (1986) Surf Coat Technol 27:117
33. Despić AR, Popov KI (1972) Transport controlled deposition and dissolution of metals. In: Conway BE, Bockris JO'M (eds) Modern aspects of electrochemistry, vol 7. Plenum, New York, pp 199–313
34. Popov KI, Maksimović MD (1989) Theory of the effect of electrodeposition at periodically changing rate on the morphology of metal deposition. In: Conway BE, Bockris JO'M, White RE (eds) Modern aspects of electrochemistry, vol 19. Plenum press, New York, pp 193–250
35. Popov KI, Pavlović MG, Jovićević JN (1989) Hydrometallurgy 23:127

36. Romanov VV (1963) Zh Prikl Khim 36:1050
37. Romanov VV (1961) Zh Prikl Khim 34:2692
38. Romanov VV (1963) Zh Prikl Khim 36:1057
39. Popov KI, Maksimović MD, Simičić NV, Krstajić NV (1984) Surf Technol 22:159
40. Vijh AK, Randin JP (1977) Surf Technol 5:257
41. Nikolić ND, Lačnjevac U, Branković G. J Solid State Electrochem doi: 10.1007/s10008-011-1626-y
42. Popov KI, Živković PM, Krstić SB, Nikolić ND (2009) Electrochim Acta 54:2924
43. Popov KI, Živković PM, Nikolić ND (2010) The effect of morphology of activated electrodes on their electrochemical activity. In: Djokić SS (ed) Electrodeposition: theory and practice, vol 48, Modern aspects of electrochemistry. Springer, New York, pp 163–213
44. Bockris JO'M, Reddy AKN, Gamboa-Aldeco M (2000) Modern electrochemistry: fundamentals of electrodics, vol 2A, 2nd edn. Kluwer Academic/Plenum, New York, p 1107
45. Wranglen G (1960) Electrochim Acta 2:130
46. Diggle JW, Despić AR, Bockris JO'M (1969) J Electrochem Soc 116:1503
47. Popov KI, Krstajić NV, Čekerevac MI (1996) The mechanism of formation of coarse and disperse electrodeposits. In: White RE, Conway BE, Bockris JO'M (eds) Modern aspects of electrochemistry, vol 30. Plenum, New York, pp 261–312
48. Popov KI, Stojilković ER, Radmilović V, Pavlović MG (1997) Powder Technol 93:55
49. Popov KI, Maksimović MD, Trnjančev JD, Pavlović MG (1981) J Appl Electrochem 11:239
50. Popov KI, Pavlović MG, Maksimović MD (1982) J Appl Electrochem 12:525
51. Pangarov NA (1964) Electrochim Acta 9:21
52. Pangarov NA, Vitkova SD (1966) Electrochim Acta 11:1733
53. Popov KI, Čekerevac MI (1989) Surf Coat Technol 37:435
54. Čekerevac MI, Popov KI (1989) Surf Coat Technol 37:441
55. Calusaru A (1979) Electrodeposition of powders from solutions. Elsevier, New York, pp 363–389
56. Mathers, Turner (1932) British Patent No. 403281
57. Mathers (1932) Met Ind (NY) 30:321, 396, 368
58. Huppomann WJ, Dalal K (1986) Metallographic atlas of powder metallurgy. Werlag Schmid GmbH, pp 21–63
59. Kudryavtsev N, Petrova A (1932) Novosti tehniki, N.K.T.R 171
60. Hardy C, Mantell C (1937) French Patent No. 814500
61. Hardy C, Mantell C (1938) US Patent No. 2157699
62. Kudryavtsev N, Tereshkocitch E (1948) Zhur Prikl Khim 12:1298
63. Borok B, Olhov I (1948) Metallurgy of powders, pp 34–35
64. Kalaida T, Rozenzweig S (1936) Collect Works Chem Cells 1:48
65. Balshin M (1935) NIIMASH 12:5

66. Mantell C (1939) British Patent No. 503306
67. Casey H (1949) US Patent No. 2481079
68. Wranglen G (1950) Acta Polytechnica Electr Eng Ser 2:69
69. Sanvordenkar K, Tendolkar G (1954) J Indian Chem Soc Ind News Ed 17:13
70. Rozenzweig S (1936) Sov avt 46284
71. Gardam G (1951) Powder Metall 6:75; (1947) Spec Rep 38:3
72. Zhelibo EP, Aryupina KA, Natanson EM (1973) Powder Metall 122:14
73. Chu CM, Wan CC (1992) J Mater Sci 27:6700
74. Fedorova O (1938) Zh Obsch Khim 8:1711
75. Hardy C, Mantell C (1937) French Patent No. 815500
76. Loshkarev M, Gernostaleva O, Kriukova A (1946) Zhur Prikl Khim 19:739
77. Levin A (1946) Zhur Prikl Khim 19:779
78. Hiruma K (1949) J Electrochem Soc Jpn 17:160
79. Drozdov B (1955) Zhur Prikl Khim 1:45
80. Nicol A (1946) CR 222:1043
81. Wranglen G (1950) Acta Polytechnica Electr Eng Ser 2:69
82. Kuroda M, Yto G, Shimizu Y (1953) Rep Sci Res (Japan) 29:429
83. Mantell C (1941) US Patent No. 2233103
84. Pavlović MG, Hadžismajlović DŽ, Popov KI (1991) Chem Ind 45:39
85. Santos JS, Matos R, Trivinho-Strixino F, Pereira EC (2007) Electrochim Acta 53:644
86. Gabe DR (1997) J Appl Electrochem 27:908
87. Palomar-Pardave M, Scharifker BR, Arce EM, Romero-Romo M (2005) Electrochim Acta 50:4736
88. Rojas M, Fan CL, Miao HJ, Piron DL (1992) J Appl Electrochem 22:1135
89. Diaz SL, Calderon JA, Barcia OE, Mattos OR (2008) Electrochim Acta 53:7426
90. Jović VD, Jović BM, Pavlović MG (2006) Electrochim Acta 51:5468
91. Jović VD, Jović BM, Maksimović V, Pavlović MG (2007) Electrochim Acta 52:4254
92. Vogt H, Balzer RJ (2005) Electrochim Acta 50:2073
93. Vogt H (1997) Electrochim Acta 42:2695
94. Vogt H (1999) J Appl Electrochem 29:137
95. Wüthrich R, Fascio V, Bleuler H (2004) Electrochim Acta 49:4005
96. Wüthrich R, Bleuler H (2004) Electrochim Acta 49:1547
97. Wüthrich R, Commninellis Ch, Bleuler H (2005) Electrochim Acta 50:5242
98. Lowenheim FA (1974) Modern electroplating, 3rd edn. Wiley-Interscience, New York
99. Jović VD, Maksimović V, Pavlović MG, Popov KI (2006) J Solid State Electrochem 10:373
100. Popov KI, Krstić SB, Obradović MC, Pavlović MG, Pavlović LjJ, Ivanović ER (2004) J Serb Chem Soc 69:43
101. Murashova IB, Pomosov AV (1989) Itogi nauki i tekhniki, Seria Elektrokhimiya, vol 30. VINITI, Moskva, p 90
102. Popov KI, Krstajić NV (1983) J Appl Electrochem 13:775
103. Lačnjevac U, Jović BM, Jović VD (2009) Electrochim Acta 55:535